

Crack coalescence morphology in rock-like material under compression

Joeun Lee · Youn Doh Ha · Jung-Wuk Hong

Received: 30 March 2016 / Accepted: 6 July 2016 / Published online: 18 July 2016
© Springer Science+Business Media Dordrecht 2016

Abstract This paper uses peridynamic simulations to determine the extent of coalescing damage and identify the underlying causes. The basic crack types and crack coalescence patterns in specimens with a flaw pair under uniaxial compression are systematically investigated. Various crack types including horsetail cracks, anti-wing cracks, and tensile wing cracks are successfully observed and the coalescence sequences are identified. By varying angles, six crack coalescence categories with respect to the overlapping ratios provide insightful information of different crack growths and indicate various cracking modes underlying various coalescence patterns. The arrangement of the flaw pair strongly influences the crack initiation position and trajectories, allowing for different coalescence morphologies. Coalescence formed by two internal tensile wing cracks, or transfixion, shows unbroken crack segments with a further loading, along with growing shear cracks until failure. In contrast, after the coalescence is formed through two horsetail cracks, the interior of the rhombic shape gets deformed with further loading. The peridynamic code adopted in this research can provide realistic simulation results and help researchers to conduct

expanded tests as well as to enhance understanding the fracture of rock-like material.

Keywords Crack coalescence pattern · Rock-like material · Crack type · Tensile wing crack · Peridynamics

1 Introduction

Rocklike material is heterogeneous, comprising of numerous micro-cracks and voids; the material therefore causes arbitrary cracks when subject to external forces including blast or earthquake. These cracks propagate along with other growing cracks and then coalesce together, thereby leading to failure or collapse of the material. Therefore, the mechanism of crack coalescence has been of great interest to many researchers in fracture mechanics. To enhance the understanding of the crack initiation and propagation of a single crack without the interaction effect of other flaws, numerous physical experiments of crack morphology in a single flaw were conducted in the articles (Bombolakis 1963; Lajtai 1974; Li et al. 2005; Wong and Einstein 2009; Vasarhelyi and Bobet 2000; Park and Bobet 2010). There is a general crack pattern in which tensile wing cracks initiate from upper and lower external tip of a flaw, or an artificially created crack, after a small movement of the upper face of the flaw under a compressive loading in Fig. 1. This slippage occurs around the center of the flaw and subsequently moves towards the

J. Lee · J.-W. Hong (✉)
Department of Civil and Environmental Engineering,
Korea Advanced Institute of Science and Technology,
Daejeon 305-701, South Korea
e-mail: jwhong@alum.mit.edu; j.hong@kaist.ac.kr

Y. D. Ha
Department of Naval Architecture, Kunsan National University,
Gunsan, Jeonbuk 573-701, South Korea

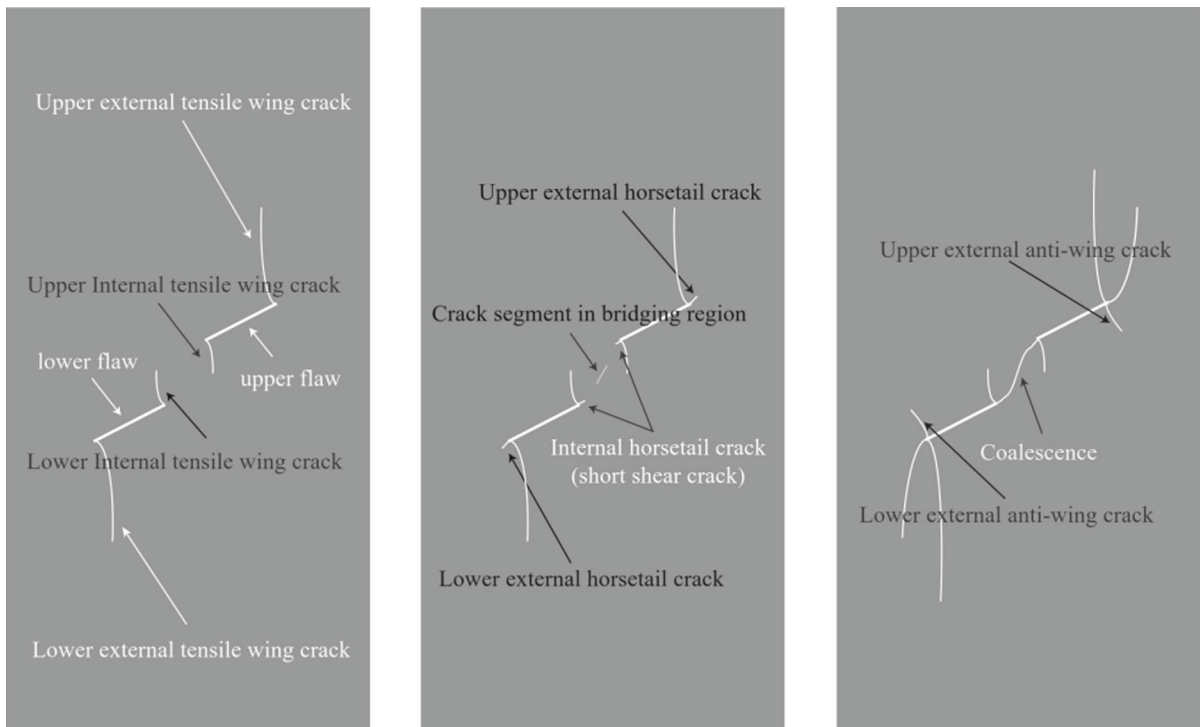


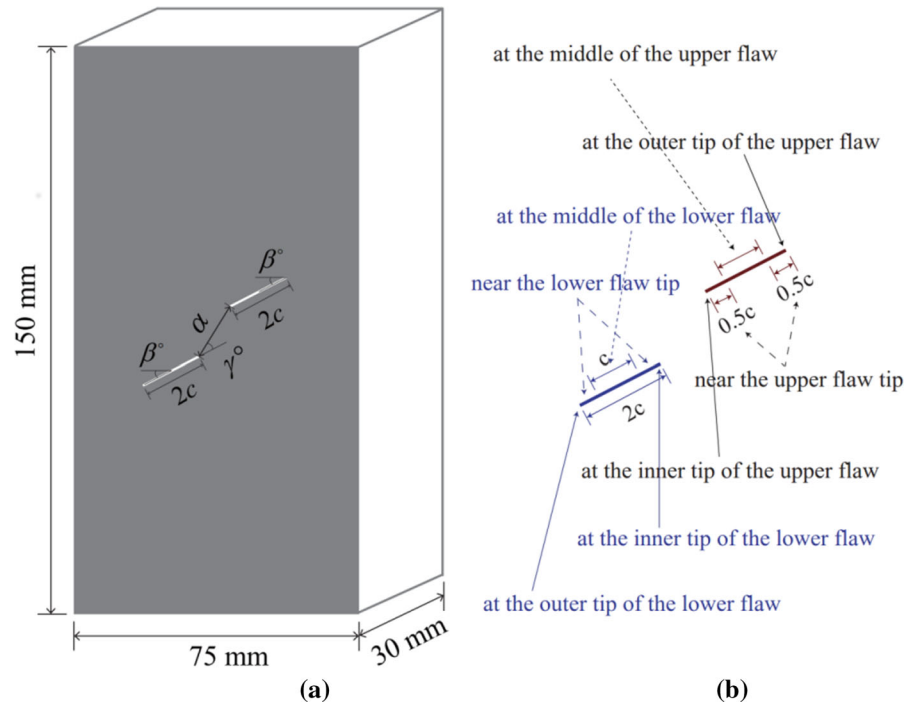
Fig. 1 Typical crack types observed in experimental results. The crack terms are for clarity modified and standardized from the articles (Ko and Kemeny 2006; Bobet and Einstein 1998; Sagong and Bobet 2002; Wong 2008)

tips of the flaw (Park and Bobet 2010). In case that the inclination angle of a flaw angle is 0 degree, the tensile wing crack initiates near the center of the flaw and propagates in a stable manner toward the loading direction, or vertically. As the inclination angle increases, the initiation position of the tensile wing crack gradually shifts toward the tips of the flaw (Park and Bobet 2010; Manouchehrian et al. 2014).

Another type of the cracks mainly observed in physical results is the secondary shear crack, which means the shear crack in general occurs followed by the tensile wing crack. In the category of the secondary shear crack, there are many confusing terms called general shear cracks (Reyes and Einstein 1991; Wong et al. 2001): for example, secondary crack (Bobet and Einstein 1998; Yin et al. 2014; Manouchehrian and Marji 2012), oblique shear crack (Cao et al. 2015), anti-wing crack (Li and Wong 2014), coplanar shear crack, quasi-coplanar shear crack (Cao et al. 2015), and horsetail crack (Li and Wong 2014). It also includes shear belt or shear zone (Lajtai 1974) where compressive stress is concentrated. Generally following the tensile wing

crack, secondary shear cracks are observed around the tips of the flaw. The shear cracks occur along with surface spalling due to the concentration of compression. This causes the shear crack to appear rough and covered with powder while tensile wing cracks are smooth and clean (Park and Bobet 2010). Hence, some researchers indicate the region which is covered with powder with surface spalling as shear belt or shear region (Lajtai 1974; Reyes and Einstein 1991). Under further loading, shear crack plays a critical role in the collapse or failure of rock material. To understand the interaction effect of two or more flaws, the crack coalescence in numerous flaw arrangements has been studied (Reyes and Einstein 1991; Wong 2008; Sagong and Bobet 2002; Park and Bobet 2009; Wong et al. 2001; Cao et al. 2015; Yang 2011). 2–10 types of linkages were identified, and it is indicated that artificially created cracks are coalesced through general shear cracks. In some types of linkages, a tensile wing crack propagates toward the other wing crack, and then joins together. However, crack coalescence in most cases is made from mixture of crack modes: tensile wing crack and shear

Fig. 2 Schematic illustration of flaw arrangement in (a) and description of initiation positions with respect to the flaw length (b), which is modified and redrawn from the article of Ko and Kemeny (2006)



crack, shear crack and shear crack, shear crack and a central tensile segment. This study aims to improve the understanding of coalescing process and its pattern through the help of the peridynamics. In Sect. 2, the key observations of previous studies about the crack patterns of a single flaw and a flaw pair are briefly mentioned. In Sect. 3, to numerically simulate arbitrary crack growth under compression, the peridynamics are briefly introduced and its numerical modeling is presented. In Sect. 4, numerical simulation results of crack coalescence are categorized by crack linkage properties along with the corresponding morphologies. Section 5 discussed all numerically observed coalescence types summarized along with their underlying characteristics. In Sect. 6, the limitation of this study and future research work are discussed. In Sect. 7, concluding remark is presented at the end of this paper.

2 Background

2.1 Previous study

Wing crack and secondary crack are uniform crack patterns in specimens with a single flaw or a flaw pair under compression. These crack patterns have

been physically or numerically investigated by many researchers. Under compression, uniform crack patterns are observed as tensile wing cracks, horsetail cracks and anti-wing cracks (Fig. 2).

Due to the small movement of the upper and lower part of the flaw under compression, tensile wing cracks initiate near or at the tips of the flaw. The tensile wing cracks initiate at the center of the flaw when the flaw inclination angle is $\beta = 0.0^\circ$ and at the tips of the flaw when the angle is higher than $\beta = 40.0^\circ$ as shown in Fig. 3. Upon further loading after the onset of the tensile wing crack, the wing cracks propagate in curvilinear path toward the loading direction. After in most cases but when in some cases the tensile cracks grow, horsetail cracks initiate from the tips of the flaw under tensile stresses but grow under shear forces. Moreover, following horsetail cracks, anti-wing cracks in some cases initiate at the tip of the flaw but in the opposite direction of tensile wing cracks. In general, tensile wing cracks propagate shorter than horsetail cracks do. As shear cracks, horsetail cracks and anti-wing cracks grow faster, then reaching the top and bottom of the specimens. Under the interaction effect of multiple flaws or a flaw pair, the growths of horsetail cracks and anti-wing cracks are critical in the collapse of materials. Therefore the interaction among these multi-cracks

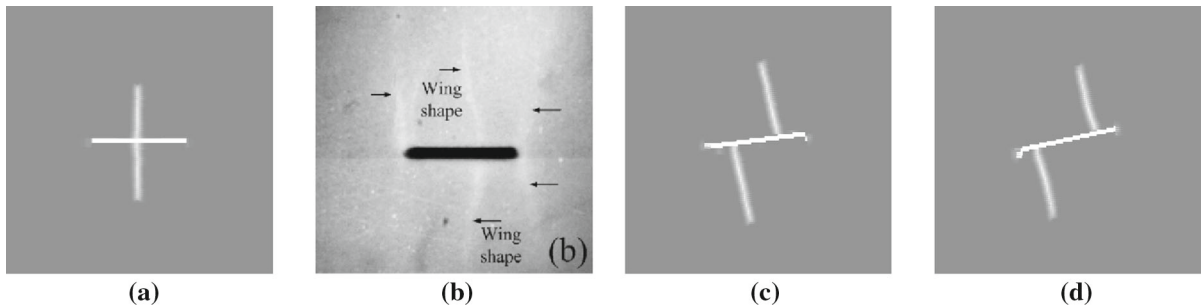
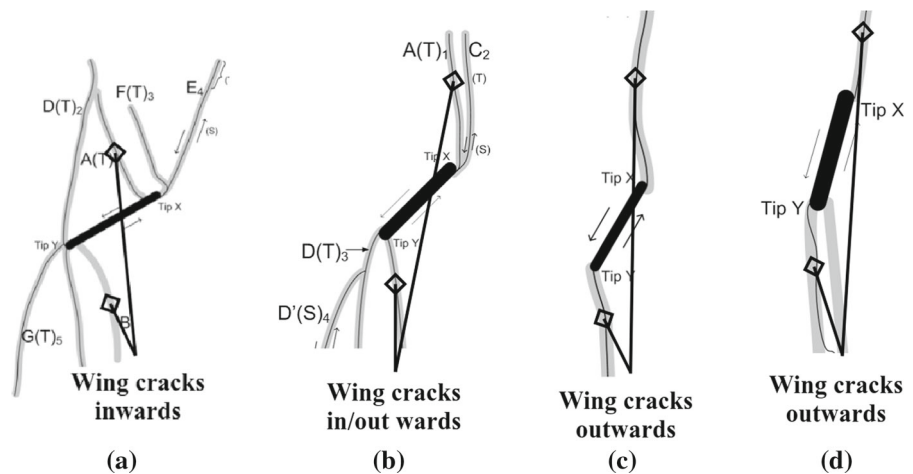


Fig. 3 Shift of the initiation position of tensile wing cracks with varying flaw inclination angles. Numerical simulation results (Ha et al. 2015) **a** $\beta = 0.0^\circ$, **c** $\beta = 7.5^\circ$, and **d** $\beta = 12.5^\circ$ and experimental result (Wong and Einstein 2009) **b** $\beta = 0.0^\circ$ in which

the tensile wing cracks initiating from the center of the flaw and the secondary shear cracks branching out from the flaw tip are observed

Fig. 4 Typical patterns of tensile wing cracks with increasing the flaw inclination angles from $\beta = 30^\circ$ to $\beta = 75^\circ$ in intervals of $\beta = 15^\circ$ in experimental results (Wong 2008). Box-arrows indicate the trajectory of tensile wing cracks along with other secondary shear cracks including horsetail cracks in **(a, b and d)**



causes the continuous degradation of its mechanical properties, thereby accelerating the failure of the specimen (Cao et al. 2015).

2.2 Basic crack types of a single flaw

The terms describing typical basic crack types experimentally observed in specimens with a single flaw under compression are for clarity shown in Fig. 3. In this paper, uniform terminology is needed because the terms have been used in many forms. In this paper, a flaw is used to denote the artificially created crack, pre-crack, or pre-existing crack. Tensile wing crack occurs after or when a small movement along the flaw (Park and Bobet 2010). Tensile wing cracks initiate at or near the tips of the flaws and propagate in a stable manner toward the loading direction. The path on which wing

cracks proceed is curvilinear or wing-like form and the pattern is influenced by the flaw inclination angle (Bobaru and Zhang 2016). If the inclination angle of a flaw is $\beta = 0.0^\circ$, the sliding occurs at the center of the flaw, causing the tensile wing cracks to initiate from the center of the flaw as shown in Fig. 3. Unlike the general crack pattern of tensile wing cracks as shown in Fig. 4, the tensile wing cracks in Fig. 3, which is created by the sliding along the flaw, proceed in a nearly vertical path, but the cracks in Fig. 3c propagate curvilinearly rather than vertically as the inclination angle increases.

Figure 3d shows the tensile wing crack initiating from the center of the flaw along with other horsetail shear cracks emanating from the tips of the flaw with further loading. Wing shapes appear like white patches which are usually observed in marble material (Wong 2008).

In case of the flaw inclination angle of $\beta = 30.0^\circ$, the initiation position of wing cracks shifts near the tips of the flaw. This shift of the initiation position of wing cracks was observed in many experimental results (Bobet and Einstein 1998; Wong 2008) and in numerical simulation results (Ha et al. 2015; Manouchehrian et al. 2014). More interesting, without changing flaw the inclination angle, this shifting mechanism is observed under the interaction effect of flaws and discussed in detail separately. The curvilinear trajectory of tensile wing cracks is obvious as the flaw inclination angle increases from around $\beta = 15.0^\circ$. The trajectory on which the tensile wing cracks of $\beta = 30.0^\circ$ propagate is curved inwardly (both toward the middle of the flaw and upwards), showing a wing-like form, like the lower tensile wing crack sketched in Fig. 4a, while the trajectory of tensile wing cracks in a single flaw steeper than $\beta = 45.0^\circ$ is curved outwardly (both toward the outer flaw tip and upwards) in Fig. 4c, d. In a flaw steeper than $\beta = 75.0^\circ$, tensile wing cracks initiate at the tip of the flaw and propagate almost in a loading direction, vertically (Wong and Einstein 2009). Therefore, during the coalescing process in a flaw pair, the trajectory of tensile wing cracks with respect to the flaw inclination angle has much effect on coalescence patterns, which is in detail discussed later. For secondary cracks, after the occurrence of tensile wing cracks, stress concentration or confinement increases at or around the tips of the flaws through the slow movement of the upper and the lower parts of the flaw. Upon further loading, pulverized areas along with spalling—an indication of high compression—appear on the surface of the regions around the flaw (Bobet and Einstein 1998).

Secondary shear cracks usually occur after tensile wing cracks appear, and the shear cracks were categorized according to their trajectories. In this paper, horsetail cracks include quasi-coplanar secondary cracks, coplanar secondary cracks. In addition, anti-wing cracks are used to denote oblique secondary cracks often used previous researchers (Bobet and Einstein 1998; Park and Bobet 2009, 2010) for the standardization of numerous confusing terms indicating secondary cracks. As shown in Fig. 4b–d, horsetail cracks initiate from the tips of the flaw or at some distance from the tips of the flaw. Sagong and Bobet (2002) described two kinds of secondary cracks: horsetail cracks and anti-wing cracks. They also described horsetail cracks as the cracks whose initiation angle is

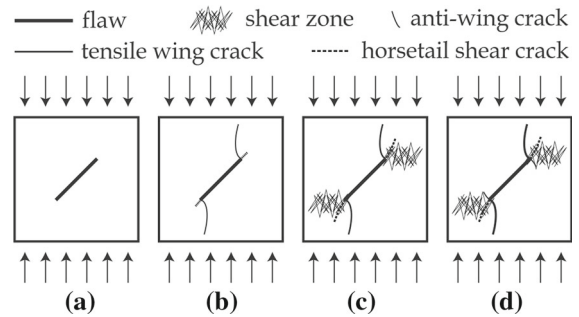


Fig. 5 General crack types observed in a single flaw in rock-like specimens. The illustration is redrawn from the experimental results (Lajtai 1974) and the crack terms are used from Li and Wong (2014)

between $\beta = 0.0^\circ$ and $\beta = -40.0^\circ$ with the respect of the flaw direction, while anti-wing cracks as the cracks whose initiation angle between $\beta = -60.0^\circ$ and $\beta = -130.0^\circ$ with the respect of the flaw direction. They presented that both horsetail cracks and anti-wing cracks initiated at the tips of the flaws where high compressive stresses are confined and spalling occurs under shear forces. However, Manouchehrian and Marji (2012) recently indicated that the horsetail cracks initiated under tensile stresses but subsequently under the influence of shear forces. These shear force would cause the surface to be rough and pulverized with powder, which indicated the slip between the faces of the flaw. Yin et al. (2014) specifically defined two types of anti-wing cracks one of which is an anti-wing crack through tensile dominant mixed mode (Ts mode anti-wing crack) and the other of which is an anti-wing crack through tensile dominant mixed mode followed by shear slippage (TsS mode anti-wing crack). Ts mode anti-wing crack is observed when the angle between the ligament line of two flaws and the horizontal line is for $\beta + \gamma = 0.0^\circ$ and $\beta + \gamma = 45.0^\circ$ as described in Fig. 2. TsS mode is observed for $\beta + \gamma = 90.0^\circ$ and $\beta + \gamma = 135.0^\circ$. The Ts mode anti-wing crack initiates at a distance away from the tips of the flaws, and then propagates downwards or upwards. The TsS mode anti-wing crack initiates at the tip of the flaw under Ts mode and then influenced by a sudden shear slippage. These two modes numerically observed in some flaw arrangements are later discussed (Figs. 5, 6).

In most articles, tensile wing cracks proceed in a stable manner and then toward the loading direction, making their trajectory curvilinear (Reyes and Einstein 1991; Bobet and Einstein 1998; Park and Bobet 2010).

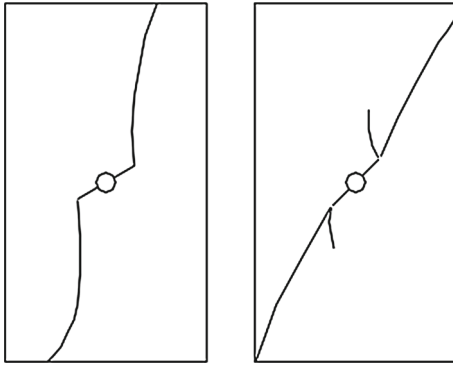


Fig. 6 Description of the trajectory of two types of crack patterns experimented by Li et al. (2005)

However, some articles observed that the trajectory of tensile wing cracks and that of horsetail cracks was skewed to left-top or right-bottom boundaries (Li et al. 2005; Yang 2011; Manouchehrian et al. 2014; Ha et al. 2015). However, less interest in the cause of this different trajectory has been still paid.


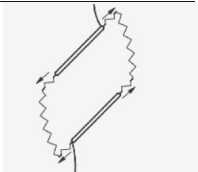
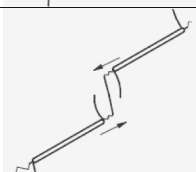
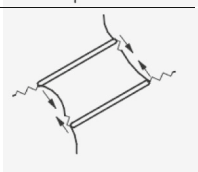
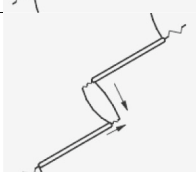
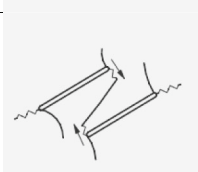
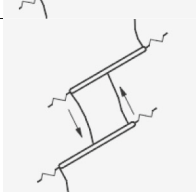
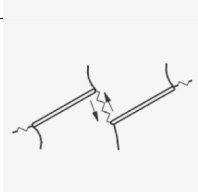
2.3 Typical coalescences patterns of a flaw pair

Reyes and Einstein (1991) observed two types of coalescence, one of which is non-persistent cracks linked through extended wing cracks under overlapping arrangement of two flaws, and the other one is crack coalescence linked by secondary cracks in case of non-overlapping arrangement. Bobet and Einstein (1998) in detail investigated the crack coalescence between a flaw pair in gypsum materials, under uniaxial and biaxial compression, varying the flaw inclination angles and the spacing between two flaws. They categorized five types of coalescences: direct shearing, initially shearing and then tension, initially shearing and then tension, only tension, shearing. They also indicated that the external wing cracks propagate longer than the internal wing cracks because the internal ones cease to growth from the onset of coalescence. Moreover, the external ones continued to reach the top and bottom boundaries of the specimens while the internal one were confined to the bridging regions, or ligament areas, between two flaws. Cao et al. (2015) indicated that crack patterns in specimens takes a turn from the propagation of tensile wing cracks to the failure of crack coalescence as the bridging angle between the inner tips of a flaw pair increases. They listed seven types of coales-

cence based on the nature of the crack involved. In case that the bridging angle is almost in the direction parallel to the compressive stress, the tensile stress path induced by relative sliding flaw surface is similar to the bridge of two flaws, leading to producing tensile wing cracks from the inner tips of the flaws. The coalescences by internal tensile wing cracks are categorized in three types: central tensile segment, direct connection of internal tensile wing cracks, and indirect connection of internal tensile wing cracks which made pull-apart zone (Crider and Peacock 2004), or transfixion plane (Cao et al. 2015), inside the coalescence. In addition, they identified three other coalescence types involving with horsetail cracks in specimens with the bridging angle of $\gamma \cong 90.0^\circ$. Zhang et al. (2015) presented five types of coalescence between two non-parallel flaws. They observed the tensile wing crack coalescence, tensile wing crack with horsetail crack coalescence, horsetail cracks, combined coalescence of tensile and shear cracks, and indirect crack coalescence. They discussed that the stress distribution in bridging region between two non-parallel flaws is more complicated and affects the types of crack initiations and their coalescence. Yang (2011) studied the coalescence between two coplanar flaws whose bridging angle is $\gamma = 0.0^\circ$. In the arrangement of two coplanar flaws is between $\gamma = 0.0^\circ$ and $\gamma = 45.0^\circ$, indirect coalescence where tensile wing crack and shear cracks (anti-wing crack or/and horsetail crack) linked together was generally observed. However, when the bridging angle is $\gamma = 60.0^\circ$ and $\gamma = 75.0^\circ$, two internal tensile wing cracks initiate from the inner tips of the flaws, propagates, and then coalesce together, showing the direct coalescence. Park and Bobet (2009), Sagong and Bobet (2002) observed several typical patterns of coalescence in specimens with a flaw pair and three flaws under uniaxial compression, which are in detail described in Table 1.

They observed that tensile wing cracks propagate and links in a stable manner when the coalescence is joined through tensile wing cracks. However, when the coalescence is made by horsetail cracks or anti-wing cracks, the coalescence process is unstable. As mentioned in Table 1, type 1 shows one horsetail crack which is coplanar to the flaw coalesce the other one in bridging region between two flaws. Both external and internal tensile wing cracks initiate at the tips of flaws and propagate toward the compressive loading direction. However, when the horsetail cracks initiate

Table 1 Schematic description of typical patterns of coalescence in experimental results with modified terms (Park and Bobet 2009)

<p>Type 1. Horsetail cracks</p> 	<p>Type 5. A horsetail crack and an out-of-plane shear crack</p> 
<p>Type 2. Horsetail cracks and out-of-plane tensile (or a central tensile segment) crack</p> 	<p>Type 6. An anti-wing crack and a tensile wing crack</p> 
<p>Type 3. A tensile wing crack and a horsetail crack</p> 	<p>Type 7. Anti-wing cracks and an out-of-plane tensile crack (or a central tensile segment)</p> 
<p>Type 4. A tensile wing crack</p> 	<p>Type 8. Anti-wing cracks</p> 

A horsetail crack denotes a quasi-coplanar secondary crack while an anti-wing crack means an oblique secondary crack. Types 1–5 is in a left-stepping arrangement of flaws, and types 6–8 is in a right-stepping arrangement of flaws

at the inner tips of the flaws, the growth of the internal tensile wing cracks is precluded. Horsetail cracks proceed in a stable manner but link together in an unstable manner, showing zigzag or kinked coalescence. In type 2, following internal tensile wing crack, horsetail cracks initiate from the inner tips of the flaws and then propagate at some distance from the tips while internal tensile wing cracks stop growing. In the bridging region, a central tensile segment (or out-of-plane tensile crack) occurs and then suddenly extends to the horsetail cracks. Regarding type 3, internal tensile wing cracks initiate and propagate along with external tensile wing cracks. Soon after that, horsetail cracks initiate from the inner tips of flaws and then coalesce with internal tensile wing cracks in a stable manner. As rhombic or sigmoidal (“S”) in shape, a pull-apart zone (Crider and Peacock 2004), or transfixion plane (Cao et al. 2015), is formed by this type of coalescence. As for type 4, each internal tensile wing crack propagates and then links the surface of the other flaw. With further loading, horsetail cracks propagate with external wing cracks growing. For type 5, horsetail cracks initiating from the tips of the flaws propagate and then coalesce with out-of-plane shear crack. The coalescence sequence appears in a sta-

ble manner, and this type of coalescence is observed in the perfectly overlapping arrangement of flaws. In case of type 6, the tensile wing cracks initiating at the tips of one flaw coalesce with anti-wing cracks growing from the other flaw. This coalescence is observed in right-stepping and high ratio overlapping arrangement of flaws. In coalescence type 7, the anti-wing crack initiating at the right tip of the upper flaw and the anti-wing crack at the left tip of the lower flaw are linked through a central tensile segment between two flaws. This coalescence is formed by sudden occurrence of a central tensile segment in an unstable manner. Type 8 shows the coalescence through anti-wing cracks initiating at the inner tips of flaws. This type is observed in low ratio overlapping or non-overlapping arrangement. Zhang and Wong (2013) categorized 8 types of coalescence from the physical experiments (Wong and Einstein 2009) and 2 types from numerical simulation. For 2a-0-0 indirect coalescence is formed through two or more cracks, and for 2a-30-30, 2a-60-0, 2a-75-0, two horsetail cracks initiating at the inner tips of the flaws and a central tensile segment are linked. They investigate various coalescences by varying the inclination angle of flaw and the bridging angle between

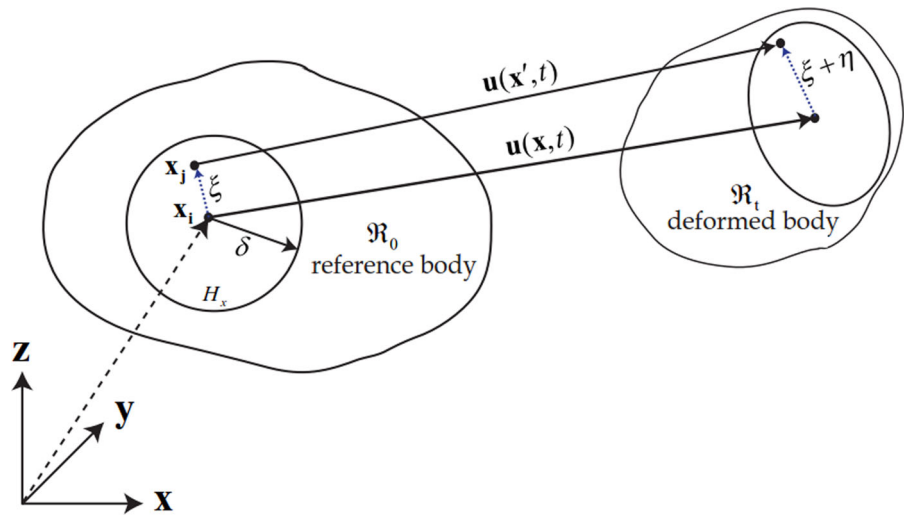
two flaws. In addition, they in detail discussed fracturing patterns coalescence with changing the bridging length between two flaws. [Li and Wong \(2014\)](#) presented 11 typical coalescence patterns and their corresponding arrangements of the flaw pair. For more systematic study, they investigated coalescence patterns in specimens with a flaw pair whose inclination angle is $\beta = 45.0^\circ$ but with 11 different arrangements of a flaw pair. In high ratio overlapping arrangements (like type 6 in [Table 1](#)), when the tensile wing crack at the right tip of the lower flaw propagate toward the right tip of the upper flaw, short shear segment, or anti-wing crack, initiate downwards from the right tip of the upper flaw. Then, the tensile wing crack propagating upwards coalesces with a short shear segment proceeding downwards. In partially overlapping arrangements (like type 4 in [Table 1](#)), the tensile wing crack initiates at the right tip of the upper flaw, and the tensile wing crack initiates at the left tip of the lower flaw. The other two cracks initiate on the inside surface of each flaw. After the two inner cracks propagate towards the opposite flaw tips, the cracks coalesce with the short shear crack segments emanating from the opposite flaw tips. In the arrangement of flaws where two inner tips of the flaws are non-overlapped (like type 8 in [Table 1](#)), two short shear cracks initiate from the inner flaw tips before shear crack segments appear in the bridging region between two flaws. With further loading, the short shear cracks coalesce with the segment, forming a continuous trajectory. When the two flaws are coplanar (like type 1 in [Table 1](#)), tensile wing cracks initiate at the flaw tips, but internal tensile wing cracks stops growing with external tensile wing cracks propagating towards the top and bottom of the specimen. Two short shear cracks initiate from the inner flaw tips and proceed towards each other. Later initiating in the bridging region, shear crack segments coalesce with the two short shear cracks, then showing the coalescence pattern as the continuous straight trajectory. In the flaw arrangement like type 2 in [Table 1](#), two inner tips of the flaws are aligned almost parallel to the loading direction. Internal tensile wing cracks propagate towards the opposite inner flaw tips, and then new shear cracks initiate from the inner flaw tips and coalesce with each other in a relatively fast manner, making the coalescence trajectory S-shaped. In a slight overlapping arrangement with respect to the loading direction like type 3 in [Table 1](#), the internal tensile wing cracks propagate in a stable manner and coa-

lesce with the inner tips of the opposite flaws. This coalescence shows an oval-like shape, or a pull-apart zone, formed solely by internal wing cracks without any shear crack. In summary, it is fully observed that the role shear cracks, including short shear crack, horse-tail crack, anti-wing crack and shear crack segment, play is critical in crack coalescence process. Therefore, this paper focuses on how these shear cracks initiate, propagate, and coalesce with other cracks and presents several typical coalescence patterns in flaw arrangements overlapped with respect to a compressive loading direction.

3 Numerical modeling

Numerical modelling provides a convenient and efficient way to predict coalescence sequences in specimens with a flaw pair under compression. In addition, the simulation method enables the effect of micro-cracks on the dynamic fracturing behaviors, in particular arbitrary cracks, to be realistically predicted. One of the advantages the numerical modelling gives is to solve the complicated problems such as the sudden growth of shear/tensile segments and TsS mode anti-wing cracks ([Yin et al. 2014](#)) and to in detail investigate fast coalescence process through the interaction of multi-cracks. Therefore, the numerical simulation results can complement insufficient physical experimental results and theoretical analyses and give insightful information to researchers in rock mechanics. Thus, numerous different numerical methods ([Wu and Wong 2012, 2014](#); [Wong 2008](#); [Manouchehrian and Marji 2012](#); [Manouchehrian et al. 2014](#); [Li and Wong 2014](#); [Zhang and Wong 2013](#); [Yin et al. 2014](#)) have been introduced for the prediction of arbitrary cracks and their coalescence. However, classical continuum theory is restrictive to calculating countless micro-cracks and propagating cracks, and it requires other mathematical models to deal with the difficulties. In addition, prior to numerical simulation the crack trajectories need to be predicted, which is not arbitrary. Some researchers ([Wu and Wong 2012, 2014](#)) recently use the Numerical Manifold method (NMM), which successfully capture basic crack patterns of a single flaw and multi-columns of parallel micro-cracks. In this paper, we use the peridynamic analysis that is effective for the investigation of rock fractures and their interactions.

Fig. 7 Illustration of peridynamic domain



3.1 Brief introduction of peridynamics

The classical, local continuum mechanics, whose linear momentum uses canonical divergence of the stress tensor, is restrictive to mathematical inconsistencies including arbitrary cracks, inborn voids, and their interaction. Peridynamics reformulates the linear momentum by incorporating integro-differential operators (Silling 2000; Silling and Askari 2005). Therefore, it is useful to predict arbitrary cracks without other mathematical methods and prior knowledge of crack trajectories (Ha et al. 2015; Ha and Bobaru 2011, 2010; Bobaru and Zhang 2016; Liu and Hong 2012a, b, c; Lee et al. 2016; Oterkus 2010; Kilic and Madenci 2010).

As expressed in Eq. 1, the linear momentum in classical continuum mechanics is reformulated with an integral operator, replacing canonical divergence.

$$\rho \ddot{\mathbf{u}}(\mathbf{x}, t) = \int_{H_{\mathbf{x}}} \mathbf{f}(\boldsymbol{\eta}, \boldsymbol{\xi}) dV_{\mathbf{x}'} + \mathbf{b}(\mathbf{x}, t) \quad (1)$$

where \mathbf{f} is the pairwise force vector, $dV_{\mathbf{x}'}$ denotes an infinitesimal volume linked to particle \mathbf{x}' , and \mathbf{b} is a prescribed body force density field, and the horizon δ controls the size of the nonlocal interaction between \mathbf{x} and \mathbf{x}' . $H_{\mathbf{x}}$ is a spherical subregion including particles within horizon δ which interact with particle \mathbf{x} and is given as

$$H_{\mathbf{x}} = \{\mathbf{x}' \in \Omega_0 : |\mathbf{x} - \mathbf{x}'| \leq \delta\}, \quad (2)$$

The pairwise force vector $\mathbf{f}(\boldsymbol{\eta}, \boldsymbol{\xi})$ in Eq. (1) is derived from a micro-elastic potential ω (Silling 2000):

$$\mathbf{f}(\boldsymbol{\eta}, \boldsymbol{\xi}) = \frac{\partial \omega(\boldsymbol{\eta}, \boldsymbol{\xi})}{\partial \boldsymbol{\eta}} \quad (3)$$

where $\boldsymbol{\xi} = \mathbf{x}' - \mathbf{x}$ is the relative position vector, and $\boldsymbol{\eta} = \mathbf{u}(\mathbf{x}', t) - \mathbf{u}(\mathbf{x}, t)$ is the relative displacement vector between points \mathbf{x} and \mathbf{x}' as illustrated in Fig. 7. A linear micro-elastic material can be obtained (Silling and Askari 2005) from Eq. 3

$$\mathbf{f}(\boldsymbol{\eta}, \boldsymbol{\xi}) = \frac{\partial \omega(\boldsymbol{\eta}, \boldsymbol{\xi})}{\partial \boldsymbol{\eta}} = \frac{\partial}{\partial \boldsymbol{\eta}} \left(\frac{c(\boldsymbol{\xi}) s(\boldsymbol{\eta}, \boldsymbol{\xi})^2 \|\boldsymbol{\xi}\|}{2} \right), \quad (4)$$

where $c(\boldsymbol{\xi})$ is the micro-modulus function, and the bond stretch is defined as

$$s(\boldsymbol{\eta}, \boldsymbol{\xi}) = \frac{\|\boldsymbol{\eta} + \boldsymbol{\xi}\| - \|\boldsymbol{\xi}\|}{\|\boldsymbol{\xi}\|}. \quad (5)$$

The corresponding pairwise force is obtained from Eqs. (4) to (5) and is dependent on a history dependent scalar-valued function, $\mu(t, \boldsymbol{\eta}, \boldsymbol{\xi})$, which are respectively defined as

$$f(\boldsymbol{\eta}, \boldsymbol{\xi}) = \begin{cases} \mu(t, \boldsymbol{\eta}, \boldsymbol{\xi}) c(\boldsymbol{\xi}) s(\boldsymbol{\eta}, \boldsymbol{\xi}) \frac{\boldsymbol{\eta} + \boldsymbol{\xi}}{\|\boldsymbol{\eta} + \boldsymbol{\xi}\|}, & \|\boldsymbol{\eta}, \boldsymbol{\xi}\| \leq \delta. \\ 0, & \|\boldsymbol{\eta}, \boldsymbol{\xi}\| > \delta. \end{cases} \quad (6)$$

$$\mu(t, \boldsymbol{\eta}, \boldsymbol{\xi}) = \begin{cases} 1 & \text{if } s(t^\alpha, \boldsymbol{\eta}, \boldsymbol{\xi}) < s_0 \text{ for all } 0 \leq t^\alpha \leq t \\ 0 & \text{otherwise} \end{cases} \quad (7)$$

The critical bond stretch s_0 is derived from the energy release rate G_f which is obtained from the energy per unit fracture area in 3D required of completely breaking all the bonds that combine two hemispheres of a body (Silling and Askari 2005).

$$s_0 = \sqrt{\frac{5G_f}{9k\delta}}. \quad (8)$$

For the numerical spatial integration of the peridynamic equations, the mid-point integration scheme is used and the peridynamic linear momentum can be expressed as

$$\rho \ddot{\mathbf{u}}_I^{(t)} = \sum_{J=1}^{N_{H_I}} \mathbf{f}(\boldsymbol{\eta}^{(t)}, \boldsymbol{\xi}) V_J + \mathbf{b}_I^{(t)} \quad (9)$$

where $\ddot{\mathbf{u}}_I^{(t)}$ is the acceleration of node I at time t , N_{H_I} is the total number of nodes within the horizon of the node I , $\mathbf{f}(\boldsymbol{\eta}^{(t)}, \boldsymbol{\xi})$ denotes the pairwise force, and $\mathbf{b}_I^{(t)}$ is the body forces of particles I at time t . As the volume of the node J , V_J is represented as $(\Delta x)^3$ with the reduction scheme (Parks et al. 2008). For numerical temporal integration of the peridynamic equation with the speed-Verlet scheme (Ercolessi 1997), the scaled force vector is expressed as

$$\mathbf{f}_v = \sum_{J=1}^{N_{H_I}} \mathbf{f}(t) V_J \quad (10)$$

The projection of the pairwise bonding force, $\mathbf{f} = c_3 s$, on the x-axis is expressed as

$$\mathbf{f}_x = \mathbf{f} \frac{|x_J - x_I|}{\|\boldsymbol{\xi}\|} = c_3 s \frac{|x_J - x_I|}{\|\boldsymbol{\xi}\|} \quad (11)$$

Derived from Eq. 11, the peridynamic stress on the cross section of the particle is projected onto the x-axis as expressed in

$$\sigma_x = \frac{1}{A_I} \sum_{J=1}^{N_{H_I}} (\mathbf{f}_x \beta_J) V_J \quad (12)$$

For the three-dimensional micromodulus and the damage index, we use the same algorithm as described in Ha et al. (2015), Liu and Hong (2012a, b, c).

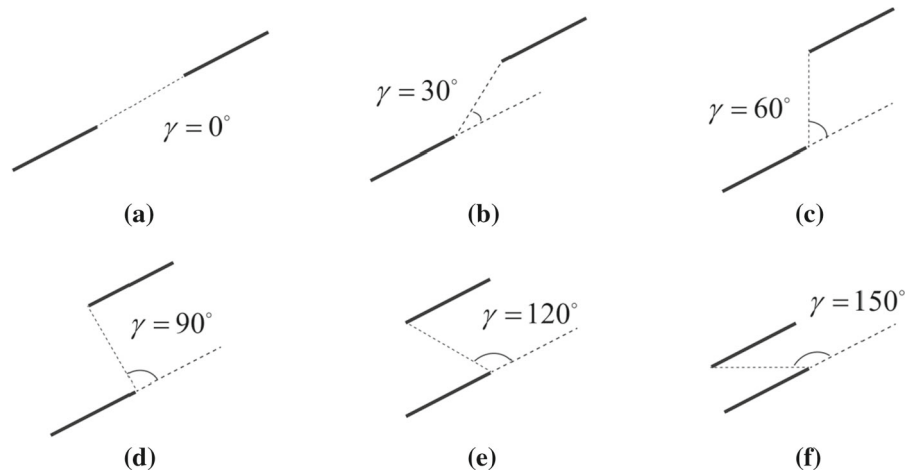
3.2 Numerical model

To realistically represent the growth of arbitrary cracks and their interactions, the peridynamic simulation implemented with parallel codes are conducted through the coupling scheme (Ha et al. 2015; Liu and Hong 2012c). As illustrated in Fig. 2a, the geometry of specimens is a 75 mm width, 150 mm height, 30 mm thickness, and the flaw is an open-through artificially created pre-existing crack of 15 mm length and 1.5 mm width. These dimensions of the specimens and flaws are followed from the physical experiments carried out by researchers (Wong and Einstein 2009; Bobet and Einstein 1998; Ko and Kemeny 2006; Wong 2008).

As described in Fig. 2a, $2c$ denotes the flaw length of 15 mm and c is half the flaw length. A flaw pair is located in the middle of the specimens. Regarding arrangement of a flaw pair, α is the bridging length between two flaws and its length is set to the flaw length of 15 mm as $\alpha = 2c$ in all specimens. β is the inclination angle of the flaw, and a flaw pair in each specimen have the same inclination angle. γ is the bridging angle between the inner tip of the upper flaw and the inner tip of the lower flaw in respect to the direction of the lower flaw. If the bridging angle is calculated in respect to the horizontal line, the angle is $\gamma + \beta$. For systematic investigation on the fracturing patterns and coalescing processes, in the arrangement of the flaw pair whose inclination angle is $\beta = 0^\circ$, the bridging angle varies from $\gamma = 0^\circ$ to $\gamma = 180^\circ$ in 15° intervals. Similarly, in every arrangement of the flaw pair whose inclination angle is from $\beta = 0^\circ$ to $\beta = 90^\circ$ in 15° intervals, the bridging angle varies from $\gamma = 0^\circ$ to $\gamma = 180^\circ$ also in 15° intervals. Thus, each arrangement of the flaw pair has 13 different bridging angles with 7 distinct inclination angles, and there are in total 91 arrangements with different inclination angles and bridging angles. The geometry of an arrangement of the flaw pair is described by three parameters, $\alpha - \beta - \gamma$ as illustrated in Fig. 2a. α denotes the bridging, ligament, distance spanning from the inner tip of the upper flaw and the inner tip of the lower flaw. The value $\alpha = 2c$ means that the bridging distance is the same as the flaw length (Fig. 8).

In this paper, the 91 specimens with discrete β s and γ s are numerically carried out and the numerical results are in detail discussed for the understanding of initiation of basic crack types, their interactions and importantly coalescing sequences. The specimen is as rock-like material whose Young's modulus is 49 GPa, density is 2700 kg/m³, and Poisson's ratio is 0.25 (Ha et al. 2015; Wong 2008). The numerical simulations are conducted with uniform grids with a grid spacing of $\Delta x = 0.25$ mm and with a horizon size of $\delta = 1.00$ mm whose corresponding m-value is set to 4 with respect to m-convergence studies given in Ha and Bobaru (2009), Ha and Bobaru (2010) for better resolution and lighter computation resources. As recommended in the article of Li and Wong (2012) in which the dynamic effect is small enough to be ignored for the low loading rates (Ha et al. 2015), the loading rate within the range of low loading rates is employed. Through the parallelization of a peridy-

Fig. 8 Schematic illustration of the flaw arrangements with the same bridging—or ligament—distance between two inner tips of the flaws and the same flaw inclination angle of $\beta = 30^\circ$, yet with the bridging angles varying from $\gamma = 0^\circ$ to $\gamma = 150^\circ$



numeric code implemented with coupling method (Liu and Hong 2012c; Ha et al. 2015), more realistic peridynamic simulation results for fracturing patterns are obtained.

4 Morphology of crack coalescence between a flaw pair

With the same bridging distance between two inner tips of the flaws, each arrangement of a pair of flaw whose inclination angle ranges from $\beta = 0^\circ$ to $\beta = 90^\circ$ in 15° intervals has 13 different bridging angles varying from $\gamma = 0^\circ$ to $\gamma = 180^\circ$ in 15° intervals.

The 91 numerical results are investigated for the initiation and growth of multiple cracks including tensile wing cracks, horsetail cracks, anti-wing cracks (Ts mode and TsS mode), and crack segments and importantly for the coalescing processes under the interaction effect of the multiple cracks in various arrangement of a flaw pair. The fracturing patterns in the results are compared with corresponding patterns physically observed in previous studies.

4.1 Coalescence patterns of zero overlapping ($\lambda = 0.00$)

In the arrangement of a flaw pair whose overlapping ratio is $\lambda = 0.0$, which is obtained from the equation of $-\{\cos(\beta + \gamma) / \cos(\beta)\}$, with respect to the loading direction as Fig. 9b, the sum of the flaw inclination angle, β , and the bridging angle, γ , is $\beta + \gamma = 90^\circ$. Described as $\alpha - \beta - \gamma$ in Fig. 2a, the arrangements

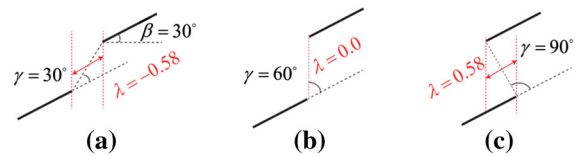


Fig. 9 Description of overlapping ratio, λ , with respect to the overlapped flaw length aligned with a vertical line, or a compressive loading direction. The negative sign stands for a non-overlapping arrangement while the positive sign stands for an overlapping arrangement

such as 2c-00-90, 2c-15-75, 2c-30-60, 2c-45-45, 2c-60-30, 2c-75-15, and 2c-90-00 are included. The 4 types of coalescence patterns are observed, and these coalescences are formed by the extension of a tensile crack segment, the growth of two horsetail cracks, the oval-like linkage of internal tensile wing cracks, the linkage of internal tensile wing cracks by increasing bridging angles.

As for the geometry of 2c-00-90 in the first row in Fig. 10, the slippage occurs around the center of the upper and lower flaw (Mughieda and Alzo’ubi 2004), causing the tensile wing cracks to initiate from the middle of the upper and lower flaw (see Fig. 1). The internal tensile wing cracks propagate longer than the external tensile wing cracks. Tensile stresses concentrated in the bridging region causes an isolated, central tensile crack segment to extend and then coalesce with the two inner flaw tips. After coalescence, the internal tensile wing cracks no longer propagate while the external tensile wing cracks propagate along with horsetail cracks growing from the outer flaw tips until fail-

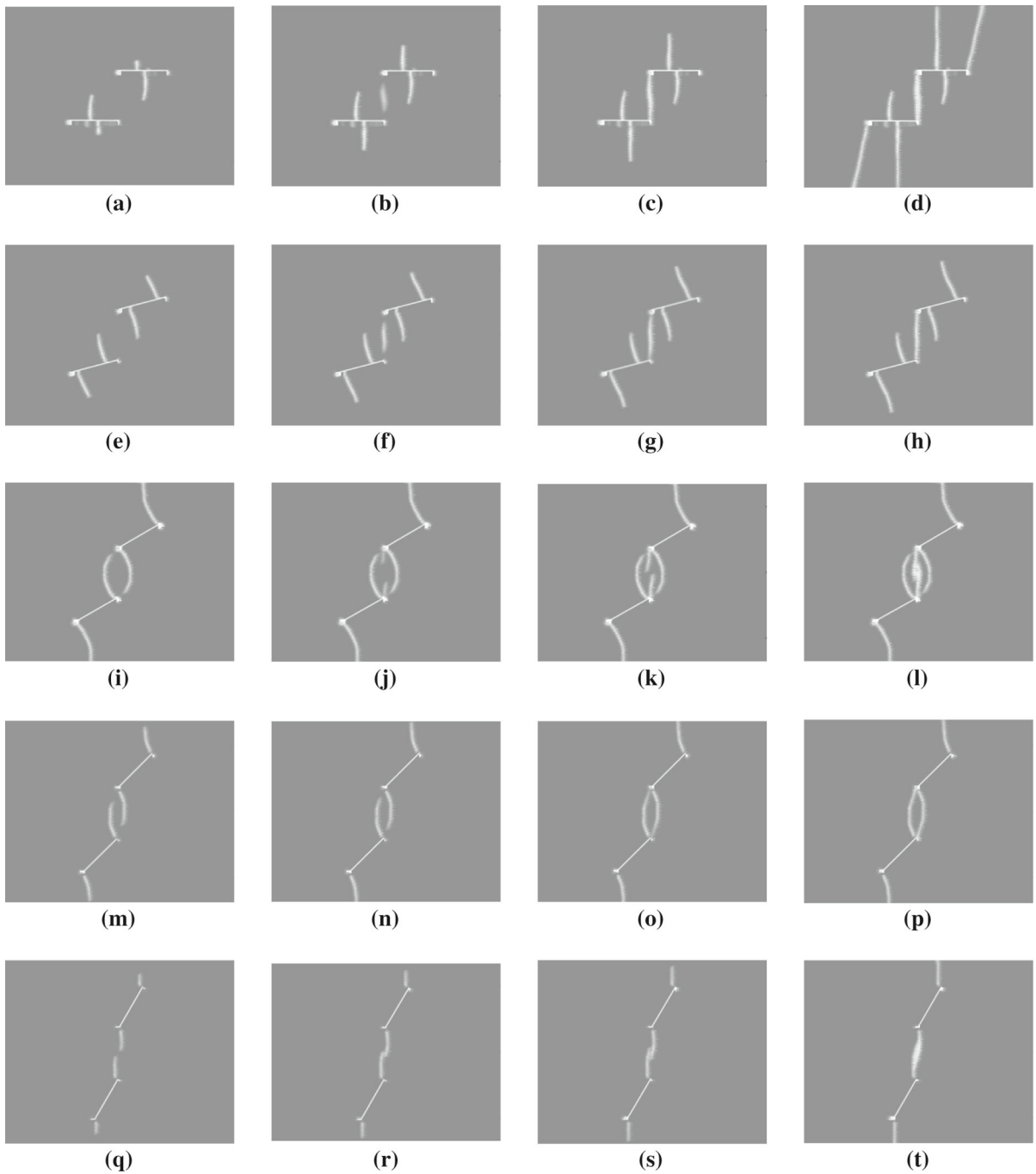


Fig. 10 Coalescence sequences in flaw arrangements with the geometry of 2c-00-90 (a–d), 2c-15-75 (e–h), 2c-30-60 (i–l), 2c-45-45 (m–p), and 2c-60-30 (m–p). For loading magnitude, **a** captured at 41.6 MPa, **b** at 44.8 MPa, **c** at 48.0 MPa, and **d** at 56.0 MPa; **e** is captured at 43.2 MPa, **f** at 44.8 MPa, **g** at 46.4

MPa, and **h** at 48.0 MPa; **i** at 60.8 MPa, **j** at 62.4 MPa, **k** at 64.0 MPa, and **l** at 67.2 MPa; **m** at 46.4 MPa, **n** at 48.0 MPa, **o** at 49.6 MPa, and **p** at 51.2 MPa; and **q** at 46.4 MPa, **r** at 49.6 MPa, **s** at 52.8 MPa, and **t** at 72.0 MPa

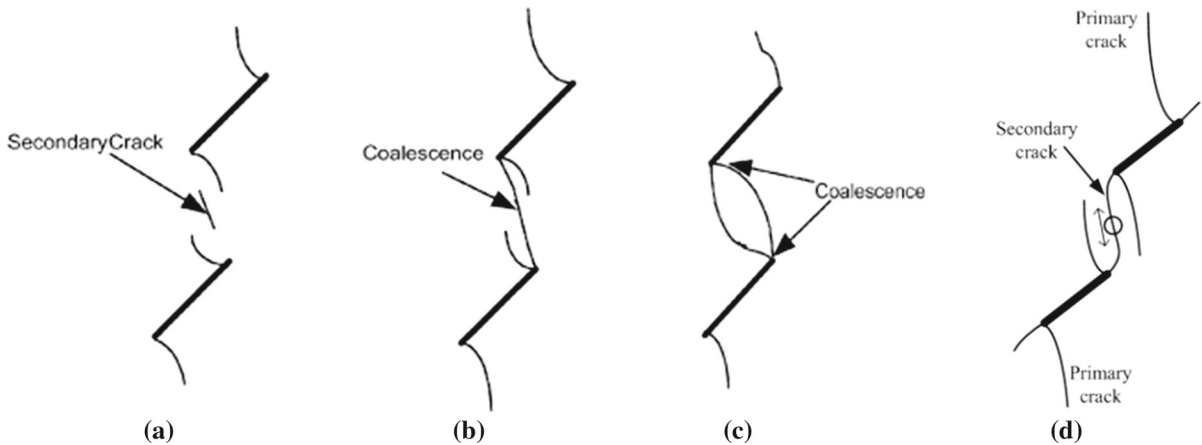


Fig. 11 Coalescences through the typical cracks in physical results (a–c) in the article of Mughieda and Alzo’ubi (2004) and d in Ref. Shen et al. (1995). a, b Show the linkage process by the extension of central tensile segments. c Shows the linkage by

the two internal tensile wing cracks. d Shows the linkage by the combination of two horsetail cracks and a central tensile segment

ure. In the coalescence pattern observed in the geometry of 2c-15-75, the tensile wing cracks initiate at the points where the first high tensile stresses (Mughieda and Alzo’ubi 2004) are concentrated. The external tensile wing cracks (see Fig. 1) initiate near the flaw tips (see Fig. 2) because the shift of the initiation position of tensile wing crack with respect to the low flaw inclination angle $\beta = 15^\circ$ as mentioned in Fig. 3. Interestingly, the initiation position of the internal tensile wing cracks shifts to the middle of the flaws because of the interaction effect in the bridging region between two inner tips of the flaws. Thus, the shift of the initiation position is subject to the effects of both the flaw inclination angle and the extent of overlapping arrangement of flaws. With growing external and internal tensile wing cracks, high tensile stresses in the bridging region (Mughieda and Alzo’ubi 2004) initiate an isolated, central tensile segment, or a central tensile crack. With a further loading, the isolated, central tensile segment extends and then links to the outer tips of the flaws as shown in Fig. 10f. After the coalescence, the internal tensile wing cracks no longer propagate, while the external ones reach the top and bottom boundaries of the specimen and the coalescence gets more deformed. Subsequently, anti-wing cracks and horsetail cracks initiate at the outer flaw tips and propagate until failure (Fig. 11).

In the arrangement of 2c-30-60 in Fig. 10i–l, the tensile wing cracks show obvious wing-like trajectory

because of the low inclination angle of the flaw. Under the interaction effect between two flaws, internal tensile wing cracks propagate more inwards and in more curvilinear path than external tensile cracks proceeding inwards and then vertically. This causes the distance between two trajectories of the lower and upper internal wing cracks (see Fig. 1) to be wider. During that time, the shear stresses concentrate at the inner tips of the flaws and initiate the horsetail cracks, or two short shear cracks (Zhang and Wong 2013). The horsetail cracks propagate each other and then coalesce through central tensile segments, which was physically observed (Mughieda and Alzo’ubi 2004). In the arrangement of 2c-45-45, the curvilinear trajectory of tensile wing cracks of $\beta = 45^\circ$ is less obvious than that of $\beta = 30^\circ$. Tensile wing cracks initiate at the tips of the flaws and grow toward the top and bottom boundaries. The path on which internal tensile wing cracks proceed is more curved than the path of external tensile wing cracks, but the distance between two internal tensile wing cracks is shorter than that of 2c-30-60. Thus, this shorter distance on which inner tensile wing cracks propagate helps the inner tensile wing cracks to coalesce each other before the initiation of horsetail cracks at the inner tips of the flaws. The coalescence formed by internal tensile wing cracks shows a pull-apart zone (Crider and Peacock 2004), or transfixion (Cao et al. 2015). In the arrangement of 2c-60-30, the tensile wing cracks initiate with the help of the high

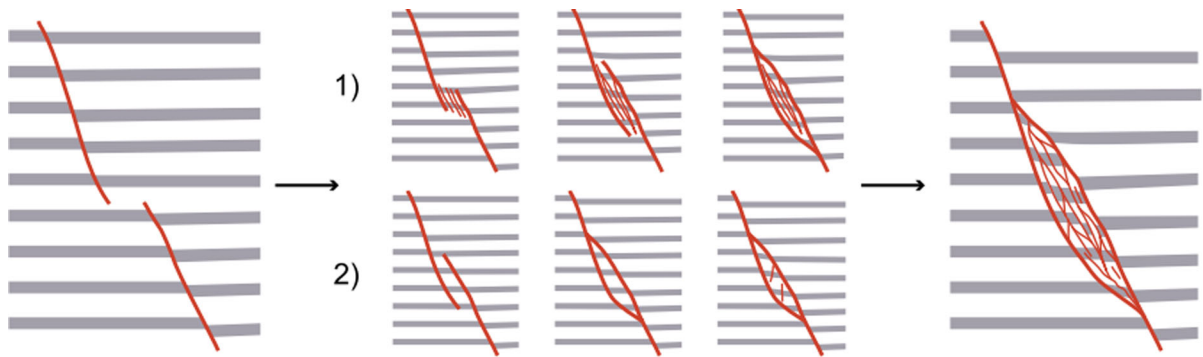


Fig. 12 Sketch of two scenarios for the development of fault-bounded lens-shaped bodies by coalescence of two preexisting faults. Scenario 1 shows the interior of the future lens is deformed before the coalescence of two propagating cracks from the flaw

tips. Scenario 2 shows the deformation of the interior of the lens after the coalescence of two propagating cracks (Van Der Zee and Urai 2005)

tensile stresses concentrated at the tips of the flaws, then growing vertically. Longer than the external tensile wing cracks propagate toward the boundaries of the specimen, each internal tensile wing crack propagates towards the inner tip of its opposite flaw. Unlike the longer distance the external tensile wing cracks propagate than that of the internal tensile wing cracks in 2c-15-75, 2c-30-60, and 2c-45-45, the internal tensile wing cracks in 2c-60-30 propagates farther. The internal tensile wing cracks meet together at the middle of the bridging region, but they do not coalesce with keeping growing. With further loading, they propagate at some distances and then coalesce together. The coalescence becomes broader until failure. According to the article of Van Der Zee and Urai (2005), the coalescence could be created by two guessing scenarios in illustrated in Fig. 12—deformation occurs before and after coalescence. Based on the observation in the numerical results in Fig. 10q–t, the deformation in the interior lens happens after the coalescence is formed by the internal tensile wing cracks initiating from the inner flaw tips, which is closer to the second scenario.

4.2 Coalescence patterns of partial non-overlapping ($\lambda = -0.27$ to -0.52)

In the arrangement of a flaw pair, the distance separated between two inner tips is 0.26 times the flaw length with respect to the vertical direction. The sum of the flaw inclination angle, β , and the bridging angle,

γ , is $\beta + \gamma = 75^\circ$, corresponding to the arrangements including 2c-15-60 ($\lambda = -0.27$), 2c-30-45 ($\lambda = -0.30$), 2c-45-30 ($\lambda = -0.37$), and 2c-60-15 ($\lambda = -0.52$), with different overlapping ratios with respect to the flaw length overlapped in the direction of the flaw (see Fig. 9). The two types of coalescence patterns are observed, one of which is formed by the short horsetail cracks initiating at the inner flaw tips and the other one of which is linked through two internal tensile wing cracks approaching each other.

In the arrangement of 2c-15-60, internal and external tensile wing cracks initiate near the flaw tips (see Fig. 2) and propagate upwards and downwards respectively. When the secondary shear cracks named horsetail cracks emanate from the inner flaw tips, the internal tensile wing cracks stop growing after their linkage with horsetail cracks. Moreover, tensile stress concentrated in the bridging region causes tensile segments to initiate away from the inner flaw tips in Fig. 13a, which was observed in Fig. 11a, b in Mughieda and Alzo'ubi (2004) and Fig. 11c in Shen et al. (1995). With the attraction of isolated, central tensile segments, the shear stresses at the inner flaw tips stimulate the nucleation of multi-microcracks, leading to forming short shear cracks at the inner tips. Upon the occurrence of these shear cracks, the cracks coalesce with the tensile segments, then showing the direct and straight crack trajectory as shown in Fig. 13b. The shear cracks approach towards and then link with the inner tip of the opposite flaw. After the coalescence, the deformation of the interior of the lens (oval-like shape) progresses. This observation is similar to the second sce-

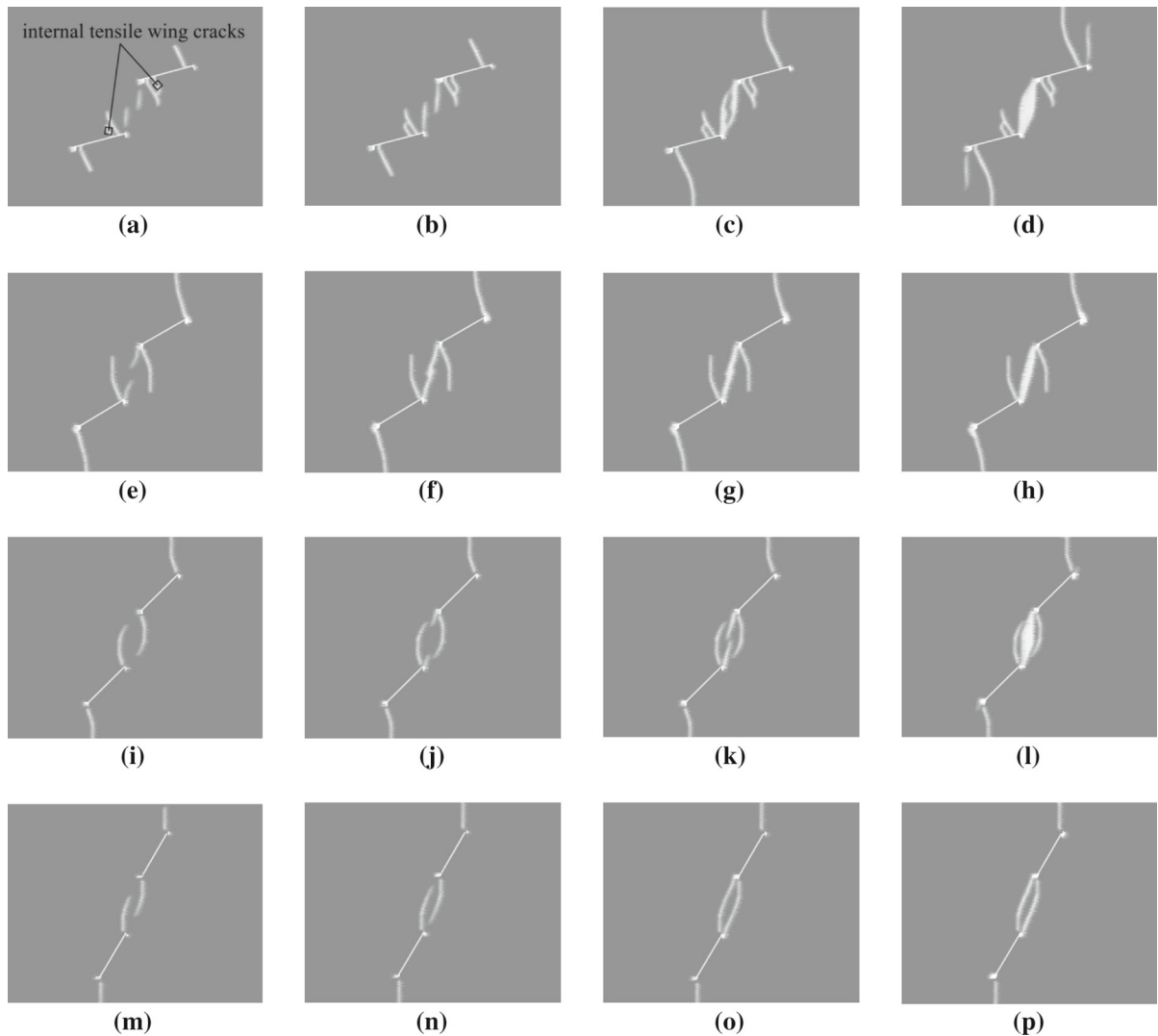


Fig. 13 Coalescence sequences in flaw arrangements with the geometry of 2c-15-60 (a–d), 2c-30-45 (e–h), 2c-45-30 (i–l), and 2c-60-15 (m–p). For loading magnitude, a captured at 41.6 MPa, b at 43.2 MPa, c at 51.2 MPa, and d at 56.0 MPa; e at 56.0 MPa,

f at 57.6 MPa, g at 59.2 MPa, and h at 62.4 MPa; i at 49.6 MPa, j at 52.8 MPa, k at 56.0 MPa, and l at 72.0 MPa; m at 49.6 MPa, n at 52.8 MPa, o at 56.0 MPa, and p at 72.0 MPa

nario proposed by the article (Van Der Zee and Urai 2005). In the arrangement of 2c-30-45, the first tensile stresses through small movement along the flaw stimulate the initiation of tensile wing cracks at the flaw tips. The tensile wing cracks propagate inwards and toward the loading direction. When horsetail cracks, or the short shear cracks, initiate at the inner tips, the internal wing cracks cease to proceed. The horsetail cracks approach each other and then coalesce into a straight crack. The straight trajectory of the linkage by

two horsetail cracks appears thicker and more obvious with a further loading (Fig. 14).

For 2c-45-30 arrangement, internal and external tensile wing cracks initiate at the flaw tips. Under the interaction effect in the bridging area, the trajectory of internal tensile wing cracks is more curved than that of external tensile wing cracks. When each internal one approaches closer to its counterpart, horsetail cracks begin to initiate at the inner flaw tips. Upon the occurrence of the horsetail cracks, the internal tensile wing

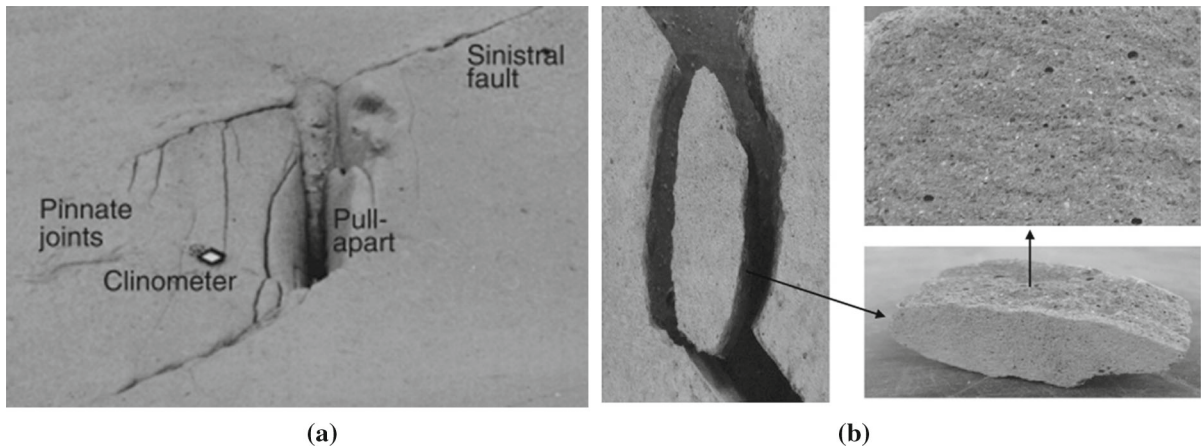


Fig. 14 **a** Photo of pull-apart zone, a slip fault zone by approaching cracks (Crider and Peacock 2004), which is closer to the scenario 1 whereby the interior of the lens becomes damaged before the coalescence (Van Der Zee and Urai 2005). **b** Transfixion plane on which no friction trace was observed. Although the bridging

area is deformed through the coalescence between two internal tensile wing cracks, there exists an unbroken segment (transfixion, rhombic shaped plane) bearing capacity against failure (Cao et al. 2015)

cracks cease to growing. Each horsetail crack propagates towards its opposite horsetail crack and soon coalesce each other. Within the boundary of internal tensile wing cracks, the coalescence formed by two horsetail cracks becomes broader with a further loading. The horsetail cracks initiate initially under tensile stresses and soon grow under shear forces (Manouchehrian and Marji 2012). It was physically observed that with the influence of shear force, the surface of the coalescence formed by two horsetail cracks appear rough and pulverized with powder. Therefore, the interior lens of the coalescence through horsetail cracks initiating at the inner flaw tips gets more deformed with a further loading, with its swelling out as observed in the first three cases including 2c-15-60, 2c-30-45, and 2c-45-30 in Fig. 13. In the arrangement of 2c-60-15, tensile wing cracks initiate at the flaw tips and propagate. External wing cracks proceed in a loading direction, but internal tensile wing cracks when approaching each other proceed in a curvilinear line. Each internal one reaches the inner tip of its opposite flaw, forming transfixion plane. Unlike the first three arrangements, 2c-45-30 arrangement shows the coalescence linked solely by two internal tensile wing cracks. The coalescence sequence through two horsetail cracks under shear forces is faster than through two internal tensile wing cracks, and shear coalescence becomes damaged with increasing loading while tensile coalescence almost stops being more deformed.

4.3 Coalescence patterns of substantial non-overlapping ($\lambda = -0.5$ to -1.0)

In the non-overlapping arrangement of a flaw pair, the distance separated between two inner tips is 0.50 times the flaw length with respect to the vertical direction. The arrangement of $\beta + \gamma = 60^\circ$ contains 2c-00-60 ($\lambda = -0.50$), 2c-15-45 ($\lambda = -0.52$), 2c-30-30 ($\lambda = -0.58$), 2c-45-15 ($\lambda = -0.71$), and 2c-60-00 ($\lambda = -1.00$) with different overlapping ratios, λ , with respect to the flaw length overlapped in the direction of the flaw (see Fig. 9). The general coalescence types numerically observed in 5 cases are, by the extension of shear segments in the rhombic shape of horsetail cracks (the first row), by the combination of horsetail cracks and a central tensile segment (in the second and third rows), and the linkage of horsetail cracks initiating at the inner tips of flaws (in the fourth and fifth rows) as shown in Fig. 15.

In 2c-00-60, tensile wing cracks initiate at the center of the flaws and then propagate towards a loading direction. When the first horsetail cracks emanate from the inner flaw tips, the internal tensile wing cracks propagate at the distance within two flaws. In addition, the secondary horsetail cracks initiate at the opposite side of the inner flaw tips at which horsetail cracks initiate. The secondary horsetail cracks grow faster than the first initiating horsetail cracks, and they proceed in a straight slant path until failure. In similarly, at the

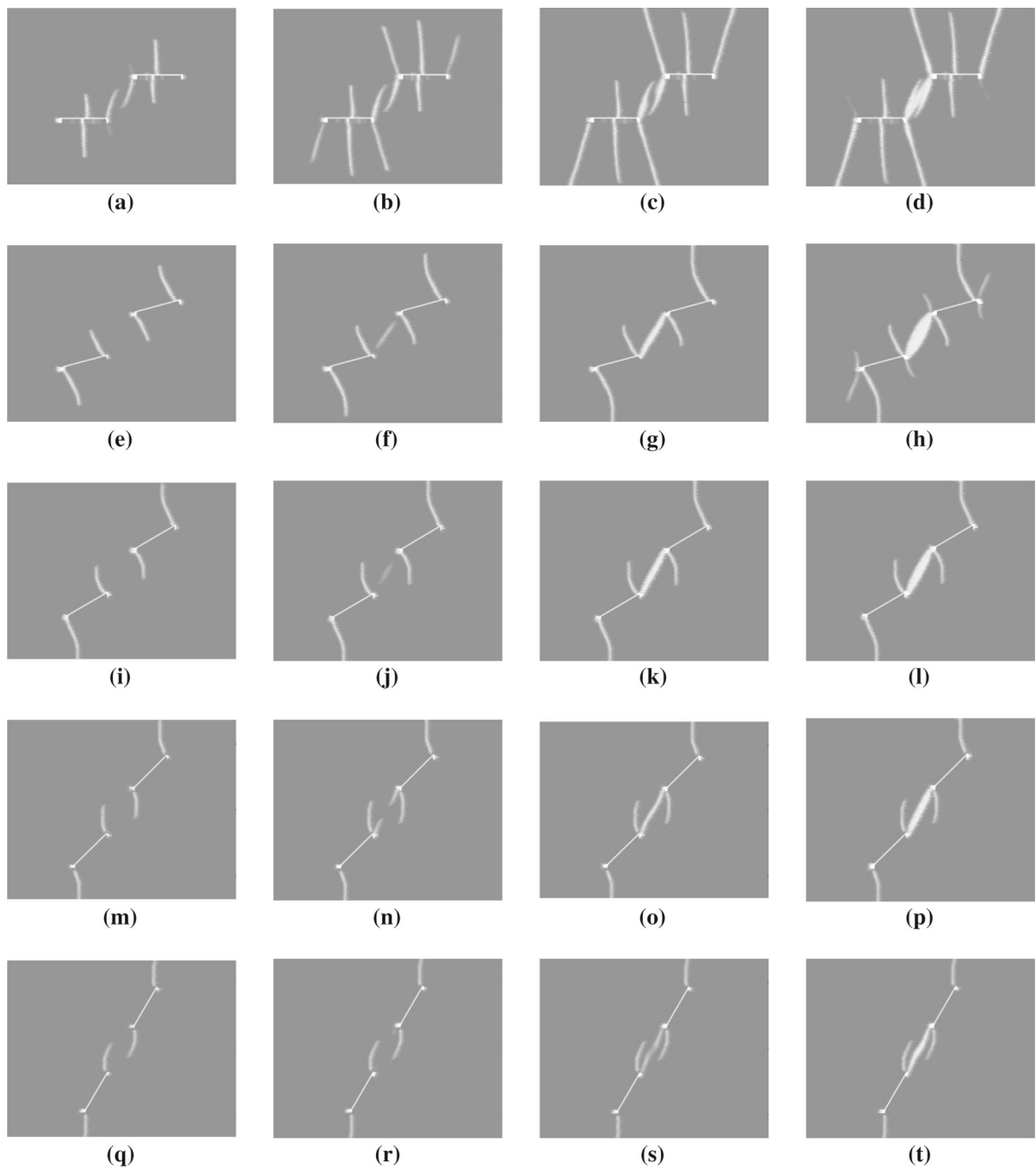


Fig. 15 Coalescence sequences in flow arrangements with the geometry of 2c-00-60 (a–d), 2c-15-45 (e–h), 2c-30-30 (i–l), 2c-45-15 (m–p), and 2c-60-00 (q–t). For loading magnitude, a captured at 48.0 MPa, b at 54.4 MPa, c at 59.2 MPa, and d at 64.0 MPa; e at 46.4 MPa, f at 49.6 MPa, g at 54.4 MPa, and h at 72.0

MPa; i at 48.0 MPa, j at 51.2 MPa, k at 56.0 MPa, and l at 64.0 MPa; m at 48.0 MPa, n at 52.8 MPa, o at 56.0 MPa, and p at 64.0 MPa; q at 56.0 MPa, r at 64.0 MPa, s at 65.6 MPa, and t at 70.4 MPa

outer flaw tips initiate the third horsetail cracks whose trajectory and the trajectory of the secondary horsetail cracks are symmetry with respect to the loading direction. In Fig. 15c, d, the first horsetail cracks approach each other and stops propagating when the shear segments occur within the lens, rhombic shape, formed by two trajectories of the first horsetail cracks. As multiple shear segments nucleate, the deformation in the lens gets more severe, showing obvious damage zone. For 2c-15-45, tensile wing cracks initiate at the flaw tips and propagate in a curvilinear path. With further loading, in the bridging region occurs an isolated, central tensile segment which subsequently is linked through horsetail cracks emanating from the flaw tips. The linkage is a straight, direct path line and under increasing loading the coalescence extends and appears like a convex lens. As loading increases, the lens deforms as Fig. 15h. Before failure, both at the outer flaw tips and at the inner flaw tips anti-wing cracks initiate with growing horsetail cracks at the outer flaw tips. At the outer flaw tips and in the opposite direction of external tensile wing crack initiate anti-wing cracks as shown in Fig. 15h. Yin et al. (2014) indicated that the mode of these anti-wing cracks is tensile dominant mixed mode followed by shear slippage in which these anti-wing cracks are termed as TsS mode anti-wing cracks. Like the coalescence sequence in 2c-15-45, the tensile wing cracks in 2c-30-30 propagate, and then the internal tensile wing cracks stop growing yet the external ones keep growing when an isolated, central tensile segment suddenly occurs. The coalescence through the mixture of a central tensile segment and two horsetail cracks is formed. The coalescence deforms like a swelling rhombic shape under increasing loading. However, at the same magnitude of loading, other different crack patterns including anti-wing cracks observed in 2c-15-45 are not captured. In the arrangement of 2c-45-15, horsetail cracks initiate at the inner flaw tips and approach each other after tensile wing cracks propagate at some distance in a curvilinear path. After the occurrence of the horsetail cracks, the internal tensile wing cracks no longer grow. It can be reasoned that the very tensile stresses which cause internal tensile wing cracks to initiate subsequently stimulate the nucleation of horsetail cracks at the inner flaw tips. The coalescence linked by the horsetail cracks is under the influence of shear forces, appearing rough and like a swelling rhombic shape, which was physically observed in Manouchehrian and Marji (2012). Like the coalescence pattern in 2c-45-15,

the pattern in 2c-60-30 shows the coalescence through approaching horsetail cracks from the inner flaw tips, and the coalescing region then becomes more obvious with a further loading. However, due to steeper flaws whose areas under the influence of compressive loading are smaller with respect to loading direction, horsetail cracks and the coalescing process happen at higher load magnitudes.

4.4 Coalescence patterns of partial overlapping ($\lambda = 0.27$ to 0.52)

In a flaw pair arrangement, the overlapping distance between two inner tips with respect to the vertical loading direction is 0.26 times the flaw length with respect to the vertical direction. The geometry in which the sum of the flaw inclination angle, β , and the bridging angle, γ , is $\beta + \gamma = 105^\circ$ includes 2c-15-90 ($\lambda = 0.27$), 2c-30-75 ($\lambda = 0.30$), 2c-45-60 ($\lambda = 0.37$), and 2c-60-45 ($\lambda = 0.52$) with different overlapping ratios with respect to the flaw length overlapped in the direction of the flaw (see Fig. 9). The uniform coalescence patterns captured in 4 different geometries of flaws is the linkage through internal tensile wing cracks. Because the trajectory of the internal tensile wing cracks is subject to the flaw inclination angle, the rhombic or sigmoidal shape of the coalescence varies from rectangular shape (2c-15-90) to linear line (2c-60-45). In 2c-15-90, the tensile wing cracks first initiate at the middle of the flaws and propagate towards the loading direction. The internal tensile wing cracks in the bridging region propagate relatively in a curvilinear path. Also the horsetail cracks at some distance from the outer flaw tips initiate and propagate vertically. With each internal tensile wing cracks approaches the inner tip of its opposite flaw, then leading to coalescence. The trajectory tip of internal tensile wing crack appears to be halt at a distance from the inner flaw tip. With further loading, the propagation tip of internal tensile wing cracks curves inwardly towards the inner flaw tips, which is due to the influence of the shear segments, at the inner flaw tips, whose length is so little that they could be overlooked in the physical experiments from the article of Li and Wong (2014). In 2c-30-75, the internal tensile wing cracks propagates towards the inner tips of the opposite flaw in a more curvilinear path than the external tensile wing crack propagating towards the vertical loading direction. The coalescence is formed by two

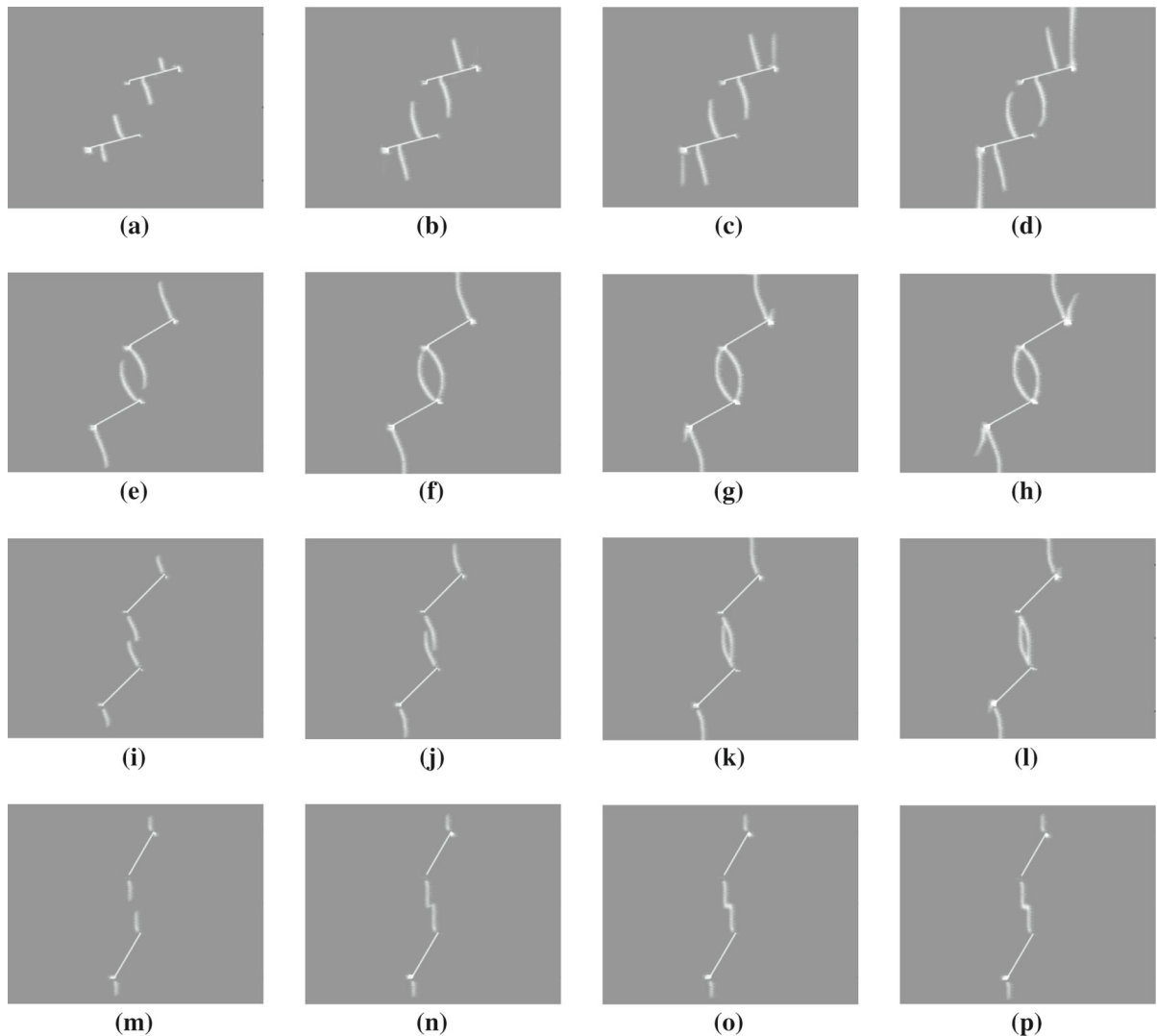


Fig. 16 Coalescence sequences in flaw arrangements with the geometry of 2c-15-90 (a–d), 2c-30-75 (e–h), 2c-45-60 (i–l), and 2c-60-75 (m–p). For loading magnitude, a captured at 41.6 MPa, b at 46.4 MPa, c at 48.0 MPa, and d at 56.0 MPa; e at 48.0 MPa,

f at 56.0 MPa, g at 64.0 MPa, and h at 72.0 MPa; i at 43.2 MPa, j at 48.0 MPa, k at 52.8 MPa, and l at 64.0 MPa; m at 51.2 MPa, n at 54.4 MPa, o at 57.6 MPa, and p at 60.8 MPa

internal tensile wing cracks as the loading increases. When the horsetail cracks at the outer flaw tips emerge, the external tensile wing cracks cease to growing but the horsetail cracks propagate towards the top and bottom boundaries of the specimen until failure (Fig. 16).

In 2c-45-60, the trajectory of the tensile wing crack of the flaw pair whose inclination angle is $\beta = 45^\circ$ is closer to the linear line than curvilinear line. The internal tensile wing cracks approach each other and coalesce with the inner tip of the opposite flaw. With further loading, horsetail cracks at the outer flaw tips

initiate and propagate until failure. In 2c-60-45, the trajectory of the internal tensile wing cracks is almost aligned with the vertical loading direction. Each internal tensile wing crack propagates towards the inner tip of its opposite flaw. However, the distance between two crack paths of approaching tensile wing cracks is short enough for the internal tensile wing cracks to be linked at the middle of the bridging region. Unlike the first three flaw arrangements in which coalescence pattern is a rhombic shape, the coalescence in 2c-60-45 appear like a connection of two lines, and there exists no shear

crack segment (Li and Wong 2014). In general, when compared with the propagating length of the external tensile wing cracks, at early stages the internal tensile wing cracks propagate longer.

4.5 Coalescence patterns of substantial overlapping ($\lambda = 0.52$ to 0.71)

In the arrangement of a flaw pair, the overlapping distance between two inner tips with respect to the vertical compression is 0.50 times the flaw length. In the arrangement of $\beta + \gamma = 120^\circ$, 2c-00-120 ($\lambda = 0.50$), 2c-15-105 ($\lambda = 0.52$), 2c-30-90 ($\lambda = 0.58$), 2c-45-75 ($\lambda = 0.71$) are considered with different overlapping ratios with respect to the flaw length overlapped in the direction of the flaw (see Fig. 9). For 2c-00-120, interestingly the internal tensile wing cracks initiate near the outer flaw tips earlier than the external tensile wing cracks initiate at the middle of the flaws. The initiation position of tensile wing cracks is different because the internal tensile wing cracks initiate at the position across the tip of the opposite flaw as shown in Fig. 17a. Therefore, the initiation position of the external tensile wing cracks shifts to at the middle of the flaws rather than typically near the flaw tips. When the internal tensile wing cracks approach at a distance from outer tips of the opposite flaw, they appear to halt. With a further loading, at the outer flaw tips horsetail cracks appear as faint lines and propagate in a relatively fast manner. During that, at the opposite side of the outer flaws initiate the TsS mode anti-wing cracks which then propagate towards the top and bottom boundaries of the specimen.

In 2c-15-105, the external tensile wing cracks initiate near the flaw tips while the internal tensile wing cracks initiate at the middle of the flaw tips. In addition, the internal tensile wing cracks propagate relatively fast. The external tensile wing cracks move in a curvilinear path, but the internal tensile wing cracks propagate almost aligned with the vertical direction. Each internal tensile wing crack propagates towards the inner tip of its opposite flaw, and with further loading proceeds near the inner tip but no longer proceeds. After the coalescence like rectangular shape is formed, the horsetail cracks initiate near the outer flaw tips. Then, the horsetail cracks propagate until failure. Horsetail cracks initiating after coalescence generally propagate relatively fast among other types of cracks.

In the arrangement of 2c-30-90, the internal tensile wing cracks propagate from the inner flaw tips and then towards the inner tip of the opposite flaw. The external tensile wing cracks initiate at the outer flaw tips and propagate in a curvilinear and subsequently in a vertical line. With further loading after the coalescence, the interior of the lens remains intact, which was an unbroken crack segment, or transfixion plane, observed in experimental results (Cao et al. 2015) as shown in Fig. 14f. For the arrangement of 2c-45-75, the crack trajectory of the internal tensile wing cracks is almost linear. The external tensile wing cracks proceed in a curvilinear line and then aligned with the vertical loading direction. The internal tensile wing cracks approach each other and then coalesce under their interaction effect at the middle of the bridging region.

4.6 Coalescence patterns of substantial overlapping ($\lambda = 0.73$ to 1.00)

In the arrangement of a flaw pair, the overlapping distance between two inner tips with respect to the vertical loading direction is 0.71 times the flaw length. The angle between the bridging line and the horizontal line is $\beta + \gamma = 135^\circ$, which corresponds to the arrangements including 2c-00-135 ($\lambda = 0.71$), 2c-15-120 ($\lambda = 0.73$), 2c-30-105 ($\lambda = 0.82$), 2c-45-90 ($\lambda = 1.00$) with different overlapping ratios with respect to the flaw length overlapped in the direction of the flaw (see Fig. 9). For 2c-00-135, like the patterns numerically observed in Fig. 17a–d, each internal tensile wing crack initiates opposite the outer flaw tip of the other flaw, later followed by its external tensile wing crack initiating at the middle of the flaws. The tensile wing cracks propagate in a stable manner, but the horsetail cracks at the outer flaw tips and the TsS mode anti-wing cracks at the opposite side propagate in a relatively fast manner. With further loading, the coalescence created through internal tensile wing cracks appear to halt while other cracks propagate until failure. In 2c-15-120 as shown in Fig. 18e–h, the internal tensile wing cracks initiate interestingly at a different initiation position, or near the flaw tip in the opposite direction. From the observation on the previous cases like Figs. 16a–d and 17e–h, the initiation position of the internal tensile wing cracks might be predicted from the position of the inner tip of the opposite flaw. Under the effect of the substantial overlapping

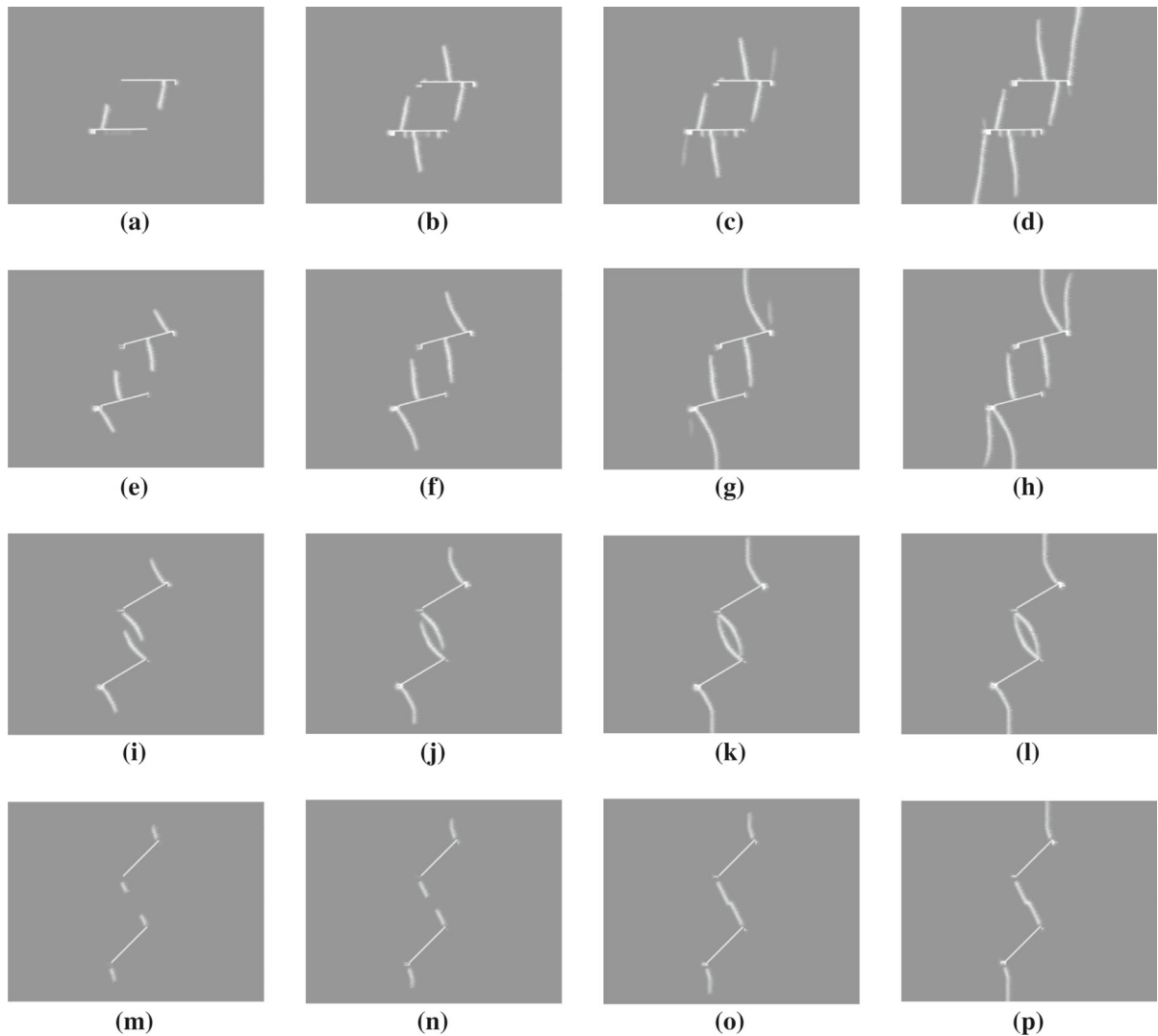


Fig. 17 Coalescence sequences in flaw arrangements with the geometry of 2c-00-120 (**a–d**), 2c-15-105 (**e–h**), 2c-30-90 (**i–l**), and 2c-45-75 (**m–p**). For loading magnitude, **a** captured at 40.0 MPa, **b** at 48 MPa, **c** at 49.6 MPa, **d** at 56.0 MPa; **e** at 44.8 MPa,

f at 51.2 MPa, **g** at 57.6 MPa, and **h** at 60.8 MPa; **i** at 48.0 MPa, **j** at 52.8 MPa, **k** at 56.0 MPa, and **l** at 64.0 MPa; **m** at 41.6 MPa. **n** at 44.8 MPa, **o** at 48.0 MPa, and **p** at 56.0 MPa

ratios and low inclination flaw angles, the initiation position of the internal tensile wing cracks might shift from the inner flaw tips far to near the flaw tips. With further loading, anti-wing cracks initiate at a distance from the outer flaw tips. The anti-wing cracks initiate not at the flaw tips but away from the flaw tips, under a tensile dominant mixed mode (Yin et al. 2014) in which these anti-wing cracks are termed as Ts mode anti-wing cracks. The anti-wing cracks propagate in a relatively fast manner upwards and downwards until failure.

In the case of 2c-30-105, tensile wing cracks initiate at the flaw tips and propagate towards the loading direction. The crack trajectory of internal tensile wing cracks is almost vertical while that of external tensile wing cracks is curvilinear. The internal tensile wing cracks propagate towards the surface of the opposite flaw. With further loading, each internal tensile wing crack coalesces with a very short secondary shear crack initiating at the middle of its opposite flaw as shown in Fig. 18k. In addition, at the outer flaw tips initiate TsS mode anti-wing cracks which propagate in a relatively

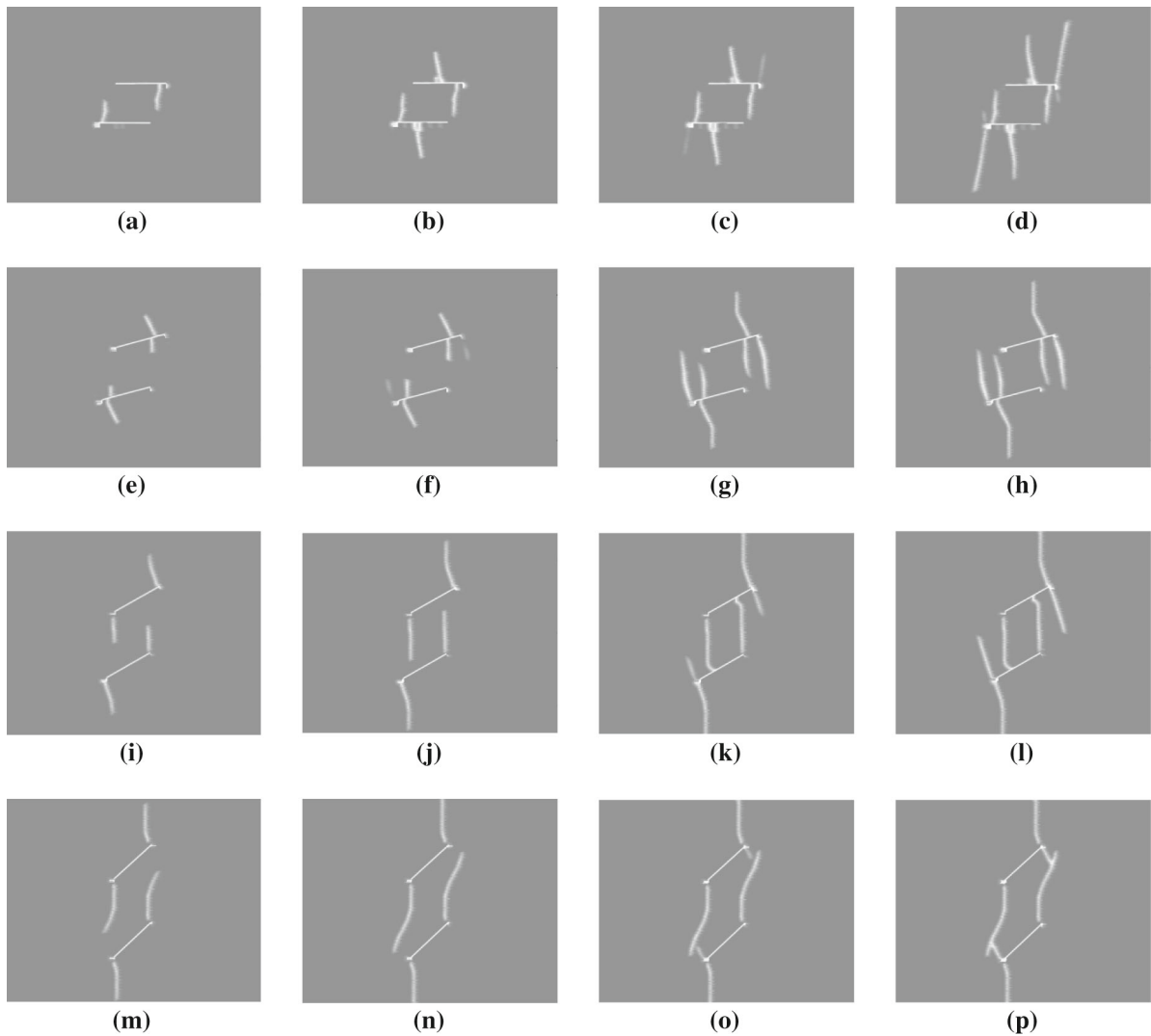


Fig. 18 Coalescence sequences in flaw arrangements with the geometry of 2c-00-135 (**a–d**), 2c-15-120 (**e–h**), 2c-30-105 (**i–l**), and 2c-45-90 (**m–p**). For loading magnitude, **a** captured at 40.0 MPa, **b** at 48.0 MPa, **c** at 49.6 MPa, and **d** at 54.4 MPa; **e** is

captured at 44.8 MPa, **f** at 46.4 MPa, **g** at 56.0 MPa, and **h** at 59.2 MPa; **i** at 48.0 MPa, **j** at 56.0 MPa, **k** at 62.4 MPa, and **l** at 65.6 MPa; and **m** at 56.0 MPa, **n** at 64.0 MPa, **o** at 72.0 MPa, and **p** at 80.0 MPa



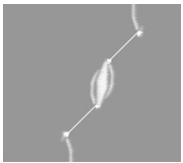




fast manner until failure. In the flaw arrangement of 2c-45-90, external tensile wing cracks propagate aligned with the vertical loading direction. Internal tensile wing cracks propagate vertically and outwards at a distance. With further loading, when the internal tensile wing cracks approach close to the outer tip of the opposite flaws, short anti-wing cracks initiate at the outer flaw tips. Then, the anti-wing cracks coalesce with the approaching internal tensile wing cracks. In the substantial overlapping flaw arrangements, the initiation position of the internal tensile wing cracks is influ-

enced under the low inclination angle of flaws. Also, anti-wing cracks play critical roles in coalescence as observed in some cases including 2c-45-90.

5 Discussion

Table 2 shows the typical coalescence patterns with respect to the flaw arrangements. In types 1–3, the coalescence formed by the horsetail cracks rather than the internal wing cracks, deforming the lens with a further

Table 2 Coalescence types of a flaw pair

Type	Coalescence pattern	Flaw arrangement	Characteristic
I		2c-00-90 2c-15-45 2c-30-30 2c-15-75	An isolated tensile crack segment in the middle of the bridging region coalesces with two short horsetail cracks.
II		2c-45-15 2c-60-00 2c-15-60 2c-30-45 2c-45-15 2c-60-00	Two horsetail cracks coalesce together. Coalescence crack surface get deformed with a further loading.
III		2c-30-60 2c-45-30	Two internal tensile wing cracks appear to halt before their coalescence. Two horsetail cracks coalesce together. Coalescence crack surface get deformed with a further loading.
IV		2c-45-45 2c-60-15 2c-30-75 2c-45-60 2c-30-90	Two internal tensile wing cracks coalesce with the inner tips of the opposite flaws. Coalescence crack surface appear to halt, though with a further loading.
V		2c-60-30 2c-60-75 2c-45-75	Two internal tensile wing cracks coalesce together in the middle of the bridging region. Coalescence crack surface appear to halt, though with a further loading.
VI		2c-15-90 2c-00-120 2c-30-105 2c-00-135 2c-15-120	The internal tensile cracks initiating near the flaws approach the inner tip of the opposite flaw but halt to propagate at a distance from the inner tip. Coalescence crack surface appear to halt, though with a further loading.
VII		2c-30-105 2c-45-90	The external tensile cracks initiating at the outer tip of the flaw coalesce with the short horsetail crack initiating at the middle of the opposite flaw. Coalescence crack surface appear to halt, though with a further loading.

loading. However, for the types 4–7 the coalescence is created by the internal tensile wing cracks, and the deformation of the lens appears to halt under further loadings.

Among the coalescence, the lens of the type 4 is a transfixion plane (Cao et al. 2015) which remains as an unbroken segment until failure through other secondary cracks. In type 6, the internal tensile wing crack stops

its propagation at some distance from the outer tip of its opposite flaw while the coalescence in type 7 is formed by the combination of the internal tensile wing cracks (which both stop at some distance like those in type 6) and the secondary cracks initiating from the surface of the opposite flaws. It is observed that the failure generally occurs through the growth of secondary cracks including horsetail cracks, anti-wing cracks, or their interactions.

6 Limitation and future work

The paper numerically studies the general crack types and coalescence in rock-like material with a flaw pair under uniaxial compression through the peridynamic reformulation. The numerical results show coalescence sequences in 91 different flaw arrangements with varying inclination angles and bridging angles, which are in good accordance with physical experimental results. The mesh used in this simulation is suitable for representing coalescing processes through the help of a parallelized peridynamic code implemented with OpenMP using multi-threading performances. It is needed to simulate better numerical results with finer mesh but at the same time to lessen heavy computational resources. This research focuses only on the arrangements with various inclination and bridging angles. Therefore, future work needs more complicated arrangements with non-parallel flaws or multiple flaws by varying bridging lengths between flaws for better understanding of the fundamental nature of rock-like material failure.

7 Conclusions

This paper numerically discusses a general morphology of crack coalescence between a flaw pair with varying flaw inclination angles and bridging angles, yet with the same bridging length. The research investigates the initiation and propagation of basic crack types between two flaws and the coalescence and interaction mechanisms of newly growing cracks in rock-like material. The following are key conclusions which can be drawn from our numerical observations.

1. In all specimens, the typical crack patterns are observed: tensile wing cracks and horsetail cracks. The external tensile wing cracks initiate near or at the outer flaw tips and then propagate towards vertical loading direction. The internal tensile wing cracks almost simultaneously initiate at the middle of, near, or at the inner flaw tips and then propagate towards the inner tip of the opposite flaw. Following tensile wing cracks, horsetail cracks initiate at the flaw tips.
2. The trajectory and initiation position of tensile wing cracks in specimens with a flaw pair are influenced under the flaw inclination as in specimen with a single flaw. This observation is shown generally in the low flaw inclination angles including $\beta = 0^\circ$ and $\beta = 15^\circ$ and interestingly in both the substantial overlapping flaw arrangements more than $\lambda = 0.50$ and the low flaw inclination angles. Moreover, at the position across the outer tips of the opposite flaw initiates each internal tensile wing crack which appears earlier than the external tensile wing cracks, coalescing with the other internal tensile wing crack.
3. The coalescence created through two horsetail cracks growing from the inner flaw tips initially appear like a direct, continuous crack path. With further loading, the interior of the coalescence swells out, showing convex-like lens. Internal tensile wing cracks appear to be halt when the horsetail crack initiate at the inner flaw tips.
4. The coalescence through the internal tensile wing cracks growing from the inner flaw tips appear like a convex-lens in cases with low flaw inclination angle, or connection line of two approaching crack in some cases with higher angle of $\beta = 60^\circ$. Unlike deformation in the interior of the coalescence, the deformation of the coalescence remains unchanged until failure is done through other horsetail cracks or anti-wing cracks.
5. In the bridging areas between two inner flaw tips, an isolated, central tensile crack segment in some cases is observed. After the tensile crack segment occurs, the short horsetail cracks initiating at the inner flaw tips then coalesce with the tensile crack segment, which is successfully captured in this numerical simulation.
6. Two types of anti-wing cracks newly reported by some researchers are also observed. Ts-mode anti-wing cracks initiate far from the flaw tips while TsS-mode anti-wing cracks initiate at the flaw tips. These two types of anti-wing cracks propagate in

a relatively fast manner, and play a major role in specimen failure.

The peridynamic simulation helps investigate the crack coalescence behavior of rock-like materials containing a flaw pair with different angles under uniaxial compression. The research reported in this paper can be used to improve the understanding of fracturing process and can serve as a basis for expanded tests.

Acknowledgements This research was supported by the Basic Science Research Program through the National Research Foundation of Korea (NRF) funded by the Ministry of Science, ICT and Future Planning (No. NRF-2015R1A2A1A01006214). This work is also supported by a grant from a Construction Technology Research Project (Development of impact/blast resistant HPRCC and evaluation technique thereof, 13SCIPS02) funded by the Ministry of Land, Infrastructure, and Transport, and by U-City Master and Doctor Course Grant Program of Korea Minister of Ministry of Land, Infrastructure and Transport (MOLIT).

References

- Bobaru F, Zhang G (2016) Why do cracks branch? A peridynamic investigation of dynamic brittle fracture. *Int J Fract*.doi:10.1007/s10704-015-0056-8
- Bobet A, Einstein HH (1998) Fracture coalescence in rock-type materials under uniaxial and biaxial compression. *Int J Rock Mech Min Sci* 35(7):863–888
- Bombolakis EG (1963) Photoelastic stress analysis of crack propagation within a compressive stress field, Ph.D. Thesis, Massachusetts Institute of Technology
- Cao P, Liu T, Pu C, Lin H (2015) Crack propagation and coalescence of brittle rock-like specimens with pre-existing cracks in compression. *Eng Geol* 187:113–121
- Crider JG, Peacock DCP (2004) Initiation of brittle faults in the upper crust: a review of field observations. *J Struct Geol* 26:691–707
- Ercolessi F (1997) A molecular dynamics primer. Spring College in Computational Physics, ICTP, Trieste, pp 24–25
- Ha YD, Bobaru F (2009) Traction boundary conditions on peridynamics: a convergence study, Technical report, Department of Engineering Mechanics, University of Nebraska-Lincoln, Lincoln, Nebraska
- Ha YD, Bobaru F (2010) Studies of dynamic crack propagation and crack branching with peridynamics. *Int J Fract* 162:229–244
- Ha YD, Bobaru F (2011) Characteristics of dynamics brittle fracture captured with peridynamics. *Eng Fract Mech* 78:1156–1168
- Ha YD, Lee J, Hong JW (2015) Facturing patterns of rock-like materials in compression captured with peridynamics. *Eng Fract Mech* 144:176–193
- Kilic B, Madenci E (2010) Coupling of peridynamic theory and the finite element method. *J Mech Mater Struct* 5(5):707–733
- Ko TY, Kemeny J (2006) Crack coalescence in brittle material under cyclic loading, ARMA/USRMS 06-930
- Lajtai EJ (1974) Brittle-fracture in compression. *Int J Fract* 10:525–536
- Lee J, Liu W, Hong JW (2016) Impact fracture enhanced by contact of peridynamic and finite element formulations. *Int J Impact Eng* 87:108–119
- Li H, Wong LNY (2012) Influence of flaw inclination angle and loading condition on crack initiation and propagation. *Int J Solids Struct* 49:2482–2499
- Li HQ, Wong LNY (2014) Numerical study on coalescence of pre-existing flaw pairs in rock-like material. *Rock Mech Rock Eng* 47:2087–2105
- Li YP, Chen LZ, Wang YH (2005) Experimental research on pre-cracked marble under compression. *Int J Solids Struct* 42:2502–2516
- Liu W, Hong JW (2012a) Discretized peridynamics for linear elastic solids. *Comput Mech* 50(5):579–590
- Liu W, Hong JW (2012b) Discretized peridynamics for brittle and ductile solids. *Int J Numer Mech Eng* 89:1028–1046
- Liu W, Hong JW (2012c) A coupling approach of discretized peridynamics with finite element method. *Comput Method Appl Mech* 245–246:163–175
- Manouchehrian A, Marji MF (2012) Numerical analysis of confinement effect on crack propagation mechanism from a flaw in a pre-cracked rock under compression. *Acta Mech Sin* 28(5):1389–1397
- Manouchehrian A, Sharifzadeh M, Marji MF, Gholamnejad J (2014) A bonded particle model for analysis of the flaw orientation effect on crack propagation mechanism in brittle materials under compression. *Arch Civ Mech Eng* 14:40–52
- Mughieda O, Alzo'ubi AK (2004) Fracture mechanics of offset rock joints: a laboratory investigation. *Geotech Geol Eng* 22(4):545–562
- Oterkus E (2010) Peridynamic theory for modelling three-dimensional damage growth in metallic and composite structures, Ph.D. Dissertation, University of Arizona
- Park CH, Bobet A (2009) Crack coalescence in specimens with open and closed flaws: a comparison. *Int J Rock Mech Min Sci* 46:819–829
- Park CH, Bobet A (2010) Crack initiation, propagation and coalescence from frictional flaws in uniaxial compression. *Eng Fract Mech* 77:2727–2748
- Parks ML, Plimton SJ, Lehoucq RB, Silling SA (2008) Peridynamics with LAMMPS: a user guide. Technical report, technical report SAND 2008-1035. Sandia National Laboratories
- Reyes O, Einstein HH (1991) Failure mechanisms of fractured rock: a fracture coalescence model. In: Proceedings 7th international congress of rock mechanics, vol 1, pp 333–340
- Sagong M, Bobet A (2002) Coalescence of multiple flaws in a rock-model material in uniaxial compression. *Int J Rock Mech Min Sci* 39:229–241
- Shen B, Stephansson O, Einstein HH, Ghahreman B (1995) Coalescence of fractures under shear stress experiments. *J Geophys Res* 100(6):5975–5990
- Silling SA, Askari E (2005) A meshfree method based on the peridynamic model of solid mechanics. *Comput Struct* 83:1526–1535
- Silling SA (2000) Reformulation of elasticity theory for discontinuities and long-range forces. *J Mech Phys Solids* 48:175–209

- Van Der Zee W, Urai JL (2005) Processes of normal fault evolution in a siliciclastic sequences: a case study from Miti, Sarawak, Malaysia. *J Struct Geol* 27(12):2281–2300
- Vasarhelyi B, Bobet A (2000) Modeling of crack initiation, propagation and coalescence in uniaxial compression. *Rock Mech Rock Eng* 33(2):119–139
- Wong LNY, Einstein HH (2009) Systematic evaluation of cracking behavior in specimens containing single flaws under uniaxial compression. *Int J Rock Mech Min Sci* 46:239–249
- Wong NY (2008) Crack coalescence in molded gypsum and Carrara marble, Ph.D. Dissertation, Massachusetts Institute of Technology
- Wong RHC, Chau KT, Tang CA, Lin P (2001) Analysis of crack coalescence in rock-like materials containing three flaws—Part I: experimental approach. *Int J Rock Mech Min Sci* 38:909–924
- Wu Z, Wong LNY (2012) Frictional crack initiation and propagation analysis using the numerical manifold method. *Comput Geotech* 39:38–53
- Wu Z, Wong LNY (2014) Investigating the effects of micro-defects on the dynamic properties of rock using numerical manifold method. *Constr Build Mater* 72:72–82
- Yang SQ (2011) Crack coalescence behavior of brittle sandstone samples containing two coplanar fissures in the process of deformation failure. *Eng Fract Mech* 78:3059–3081
- Yin P, Wong RHC, Chau KT (2014) Coalescence of two parallel pre-existing surface cracks in granite. *Int J Rock Mech Min Sci* 68:66–84
- Zhang XP, Liu Q, Wu S, Tang X (2015) Crack coalescence between two non-parallel flaws in rock-like material under uniaxial compression. *Eng Geol* 199:74–90
- Zhang XP, Wong LNY (2013) Crack initiation, propagation and coalescence in rock-like material containing two flaws: a numerical study based on bonded-particle model approach. *Rock Mech Rock Eng* 46:1001–1021